Shape optimization of the time-harmonic response of vibroacoustic devices using cut elements

Dilgen, Sumer B.; Jensen, Jakob S.; Aage, Niels

Published in:
Finite Elements in Analysis and Design

Link to article, DOI:
10.1016/j.finel.2021.103608

Publication date:
2021

Document Version
Peer reviewed version

Citation (APA):
Dilgen, S. B., Jensen, J. S., & Aage, N. (2021). Shape optimization of the time-harmonic response of vibroacoustic devices using cut elements. *Finite Elements in Analysis and Design*, *196*, Article 103608. https://doi.org/10.1016/j.finel.2021.103608

Shape optimization of the time-harmonic response of vibroacoustic devices using cut elements

Sumer B. Dilgen[a,b,*], Jakob S. Jensen[a,c], Niels Aage[a,c]

[a] *Centre for Acoustic-Mechanical Micro Systems (CAMM), Technical University of Denmark, 2800 Lyngby, Denmark*
[b] *Acoustic Technology, Department of Electrical Engineering, Technical University of Denmark, 2800 Lyngby, Denmark*
[c] *Solid Mechanics, Department of Mechanical Engineering, Technical University of Denmark, 2800 Lyngby, Denmark*

Abstract

This article presents a method for generalized shape optimization of time-harmonic vibroacoustic problems. The modeling approach utilizes an immersed boundary cut element method in conjunction with a level set representation of the geometry. The cut element method utilizes a fixed background mesh, a dimensionless contrast parameter and an integration scheme to realize complex geometries and obtain accurate physical solutions to the governing problem. The design parameterization is obtained using a nodal level set description, directly linked to the mathematical design variables, and the gradients of the objective and the constraints are obtained with the discrete adjoint approach. The framework is applied to the optimization of three 2D examples. A study on the effect of initial guess for the proposed optimization procedure is presented on a benchmark example of the design of an acoustic partitioner. Further optimization examples include design of a wave splitter to realize prescribed frequency dependent directivity for emitted acoustic waves and a suspension structure design to improve the performance of a simplified 2D model of a hearing instrument. The results demonstrate that, even though the final topology is strongly dictated by the initial design, modifying the shape allows for a significant improvement of the system behavior.

Keywords: Vibroacoustics, Cut finite elements, Immersed boundary methods, Level set methods, Shape optimization

1. Introduction

Topology optimization has become a widely utilized tool in the design of engineering products since its introduction in the late 1980's [1, 2]. Essentially the optimization process seeks to minimize a given objective function by distributing material in a certain design domain. Primarily it has been utilized in the design of elastic structures to realize stiff but lightweight designs [3]. Nowadays, the scope of application areas of topology optimization is ever widening and includes different physics, e.g., computational fluid dynamics (CFD) [4, 5] and acoustics [6, 7]. To allow for maximum design freedom, and to ensure differentiability of the parameterization enabling the use of gradient based optimizers, density based topology optimization is a popular choice. In this method the material distribution problem is relaxed and the material properties are interpolated between solid and void phases. However, issues regarding the physical interpretation of the gray areas (material realizations between solid and void phases) under certain conditions remain a problem, e.g., regarding design dependent pressure loads [8] where it could be hard to identify the design boundary due to the presence of intermediate phases. Although advanced projection methods and filtering approaches have been developed to eliminate intermediate density elements [9, 10, 11, 12], these methods at best provide a crisp stair-case boundary description. Furthermore, in multi-physics optimization cases, a clear and exact interface description is crucial for the physics that are coupled through a boundary, since generally such strongly coupled physics exhibit a high

*Corresponding author

Email addresses: sydil@elektro.dtu.dk (Sumer B. Dilgen), jsj@mek.dtu.dk (Jakob S. Jensen), naage@mek.dtu.dk (Niels Aage)

degree of sensitivity to small design variations, e.g., fluid-solid interactions. This behaviour makes the utilization of density based topology optimization a challenge due to its "pixelated" interface representation. In certain cases, such as for strongly coupled acoustic-mechanical systems, the presence of unwanted intermediate phases in the final design may contribute strongly to the end performance. Here, the post-processing step of converting the pixel design data to a body fitted mesh, may lead to loss of features in the optimized design. The effect can be that the removal of these artificial gray elements causes disappearance of resonance peaks, shifts in resonance peaks and leads to dramatic changes in the overall dynamic response when evaluated with a body-fitted mesh arrangement [13].

As an alternative to density based methods, level set type methods [14, 15, 16, 17] also allow for almost free form design evolution superior to pure shape optimization, in the sense that avoiding self-intersecting surfaces, enforcing curvature control, etc. are much simpler to handle by level set methods. For a given design iteration, boundary description is typically given from the zero level contour of the level set function. In terms of modeling the physics, ersatz material models (well known in density based topology optimization) may be used [18, 19]. Here, the geometry description given from the level set function is mapped to piecewise constant density elements and the interface is realized by interpolated gray elements. This approach exhibits challenges in modeling similar to density based methods due to the interface representation. To preserve well-defined boundaries throughout the optimization, body fitted meshes are also commonly used to capture the physics [20]. However, this approach requires a re-meshing step between every design cycle. The application of body fitted meshes provides a structure that is well described with a clear boundary description. Hence the method is inherently suitable for design problems which show a high degree of sensitivity to the description of boundaries, e.g., resonators and scatterers as often encountered in vibroacoustic design problems. The application to optimization of coupled acoustic-structural systems with body fitted meshes can be found in the works of [21, 22, 23]. For modeling of crisp and well-defined boundaries, instead of utilizing re-meshing strategies, immersed boundary methods such as CutFEM and X-FEM [24, 25, 26] have also shown great promise. These methods facilitate the modeling of complex geometries that do not conform to the fixed background mesh. Utilization of a fixed mesh for the modeling and optimization avoids the costly operation of re-meshing the evolving interface at each design iteration. Moreover, these modeling approaches also avoid possible numerical noise on the sensitivities [27] that may arise due to re-meshing procedures and interpolations between the background optimization mesh and the fitted mesh. Recently, the CutFEM method is utilized in the work [28] for the level set based shape optimization of a 2D acoustic horn.

For optimization, the shape evolution of the boundary in the classical level set approach, although several variants of the method exist, is based on the solution of a Hamilton Jacobi type equation (or a reaction-diffusion type equation) which uses the shape sensitivity of the design boundary to move the interface. Different from the classical level sets, this paper utilizes the so-called explicit or parametric level set method for the optimization process [29, 30]. In this approach, the level set field is not required to be a signed distance function as in the classical approach. Instead a scalar valued description, much like density based methods, is used. The level set values are directly tied to the mathematical design variables through a sequence of filter operations, which allows the method to facilitate design updates with the use of standard nonlinear programming tools instead of solving the Hamilton Jacobi equation to propagate the design boundary. This also increases the generality of the optimization approach by allowing a straightforward inclusion of multiple constraints and different optimization formulations such as min-max problems. The explicit level set method along with X-FEM and CutFEM have been utilized for structural optimization in the work of [31, 32] and multi-physics frameworks such as [33, 34]. Since the design is evolved from the interface, usually shape optimization based on level sets exhibits strong dependence on the initial configuration. To allow for holes to appear during the design iterations, either topological derivatives [35] or hole insertion algorithms which evaluate the design for a suitable criteria to insert holes [36] can be used. For a thorough comparison of topology optimization formulations with density, level set, and evolutionary-based methods for vibroacoustic problems, we refer to the recent review paper [13].

In this work we present a novel crisp interface, fixed background mesh, explicit level set based, generalized shape optimization method for time-harmonic coupled acoustic-structural systems. We remark that other approaches based on explicit level set design representations, often are denoted as level based topology optimization methods, e.g. [30]. However, we argue that any boundary evolving design methodology without a hole insertion and/or a material seeding scheme, presents less design freedom than that of the classical density based topology optimization, and hence motivates the distinguishment. However, in our case the benefits of an exact and accurate boundary representation motivate the use of a boundary evolving method. That is, for many multi-physical problems, including vibroacoustics, an accurate representation of the coupling interface is paramount to properly model the physics [37]. To this end, a cut element method is used for discretizing the multi-physical PDE and the chosen approach can to some extent be viewed as a special case of either of the following methods: CutFEM [25] without stabilization, XFEM without enrichments [38] or the Finite Cell method [39]. In this work we adopt the cut element approach to shape and topology optimization as proposed in [40] and extend it to include acoustic-structural coupling. In a related (and parallel) publication the same approach is applied to transient vibroacoustic problems [41]. The paper is organized as follows: The level set design parametrization is described in section 2. Section 3 describes the governing equations along with detailed implementation aspects of the utilized cut element method. Sensitivity analysis regarding the utilized discrete adjoint method is described in section 4. Finally, in section 5 the developed framework for the shape optimization of vibroacoustics systems is demonstrated with three 2D examples.

2. Geometry description

2.1. Level set method

Throughout this work a scalar valued (level set) function $\bar{s}(x)$ of the following form is utilized to define the regions occupied by the structure and the acoustic domains:

$$\begin{aligned} &\bar{s}(x) > 0, && x \in \Omega_s \text{ (structural domain)} \\ &\bar{s}(x) = 0, && x \in \Gamma_{as} \text{ (interface)} \\ &\bar{s}(x) < 0, && x \in \Omega_a \text{ (acoustic domain)} \end{aligned} \tag{1}$$

The utilization of the above function provides a simple approach to capture complex geometries with a natural way of tracking the interface between two physical domains. Here, the structural domains are embedded within the positive valued regions of the level set function whereas the acoustic domains are defined with the negative valued regions. The acoustic-structure interface Γ_{as} is always captured clearly from the zero iso-curve which carries importance in terms of the modeling of physics that are strongly coupled through the interface. Figure 1 illustrates an example of employing a scalar valued function to describe a design topology of embedded acoustic and structural domains. Contrary to classical level set methods, the chosen parametric level set representation is not based on a signed distance function, but instead the level set field is bound in the interval $\bar{s}(x) \in \{0, 1\}$. This choice will be further explained and motivated in the upcoming section.

2.2. Level set parametrization

For parametrization we define a set of design variables $\mathbf{s} = \{s_1, s_2, \cdots, s_n\}^T$ and link these to the physical level set field $\bar{s}$ that describes the geometries of the coupled system. The design variables are defined on the nodal points of a fixed grid. We define $\mathbf{s}$ within the range of $0 \leq s_i \leq 1$ for the following reason. First, this bound allows the utilization of gradient based optimizers in a similar manner as for standard density based topology optimization. Although the bounds on the design variables can be chosen in arbitrary ranges, their role is to introduce a scale on the design sensitivities which effects the course of the optimization. That is, the bounds together with the convolution filter presented next, impose an upper bound on the gradient of the level set field. This leads to the second reason for introducing the bounds, which is that by linking the bounds on the physical level set field to the size of the elements in the background mesh, it is possible to achieve a numerically stable optimization process. The reader is referred to Coffin and Maute [42] and Andreasen et. al. [40] for a detailed discussion of this choice. Hence, the mathematical design variables are first mapped to the bounds corresponding to half the element size $-0.5h_e \leq \tilde{s}_i \leq 0.5h_e$, where $\tilde{s}_i = (h_e s_i) - 0.5h_e$. Next, in order to ensure regularity on the optimized designs and to impose the upper bound on the level set gradient, as well as to extend the region of influence of the otherwise localized sensitivities, the mapped design variables $\tilde{\mathbf{s}}$ are smoothed before extracting the zero-level contour. For this operation,

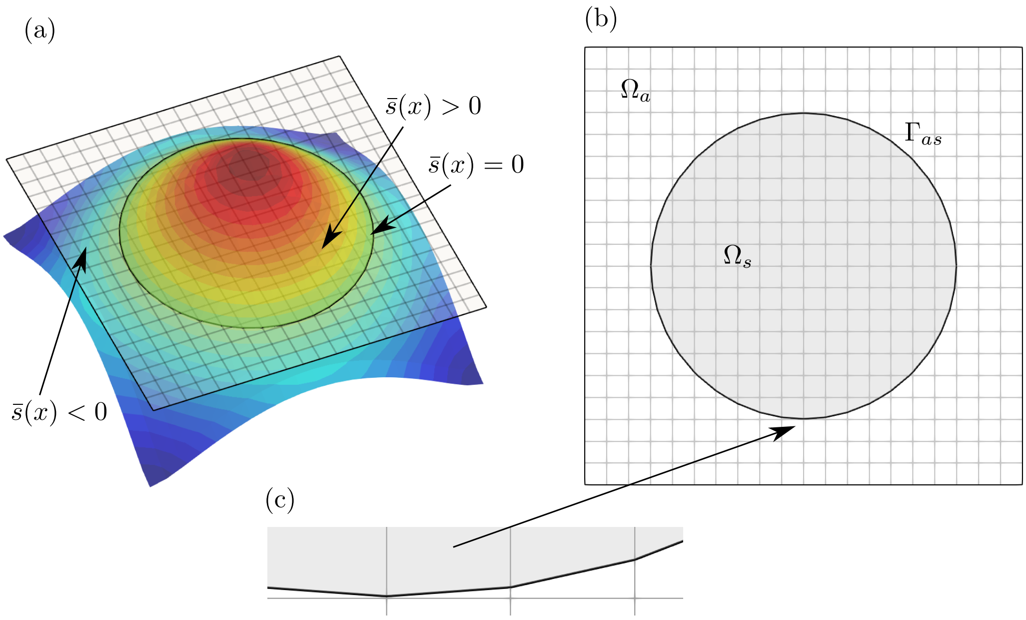

Figure 1: The level set function and its embedding physical domain: (a) the regions that are implicitly defined based on the values of the level set function are illustrated, (b) shows the utilized finite element mesh along with the realized structure from the zero iso-curve of the level set function, (c) interface is realized with straight lines across elements.

the following pde-type filter [43] is employed:

$$-r^2\nabla^2\bar{s} + \bar{s} = \tilde{s} \tag{2}$$

To ensure a stable solution of the above pde-type filter irrespective of the given filter size r, a cell centered finite volume method is employed for the discretization of Eq. 2. Remark, if the filter equation was solved using standard Galerkin finite elements, a lower bound for the radius exists for which smaller choices of r would lead to violations of the input variable bounds. Due to the cell centered finite volume approach, the nodal mapped variables $\tilde{\mathbf{s}}$ are interpolated to cell centers, i.e., $\tilde{\mathbf{s}}_c$ where subscript c denotes discrete variables defined on the cell center. Similiarly, after calculating the solution of the pde filter, the cell centered level set values $\bar{\mathbf{s}}_c$ are interpolated back to nodes of the element and describe the geometry that is used in the analysis, i.e., $\bar{\mathbf{s}}$. We remark, that interpolating between cell centers and nodal points provide an additional intrinsic filter effect which smoothens the boundaries even when using a filter radius $r = 0$. Similar approaches to parametrize a level set function have been used in the literature, e.g., by using radial basis functions or convolution type filtering [44, 45]. It is noted that usage of such parametrizations, including the parameterization used for this work, does not ensure minimum feature sizes as it does in density based topology optimization. Hence, the only noticeable difference in the chosen design parametrization compared to [40], is that the present work does not include a minimum feature size control. This is deemed reasonable as the focus of this work is on the proposed modelling approach for the optimizatio of strongly coupled vibroacoustic problems, and not specific engineering design problems with given manufacturing constraints.

In this work, the same mesh is used to discretize the level set function and for the finite element analysis. Figure 1(b) illustrates the coupling boundary Γ_{as} between acoustic and structural domains intersecting finite element edges. The modeling of the non-conforming boundaries on a fixed mesh is done using an immersed boundary cut element method [40]. Instead of re-meshing the interface, the boundary representation is obtained through a special integration scheme for the elements that are cut by zero contour of the physical level set field. The non-conforming boundary is represented by straight lines (2D) across elements (Fig. 1(c)) as the level set function is discretized by linear shape functions. It should be noted that the chosen design parameterization does not prohibit sub-element features by construction, i.e. double cuts are possible. However, our numerical experiments have shown that double cuts do not constitute a significant problem in the sense that they do not occur as long as a fine enough mesh is used to describe the geometry. That is, our numerical experiments have shown that as long as the underlying finite element mesh is fine enough to accurately resolve the structural vibrations, i.e. the wavelength, we have not seen any instances of double cuts. However, it should be emphasized that this rule-of-thumb is a heuristic and cannot guaranty suppression of double cuts in general. This could, however, be guarantied by including length-scale control as done in e.g. [12, 40] The only major numerical issue concerning the proposed modelling of cut elements arise when a non-conforming boundary intersects exactly or in very close proximity to a background mesh node. This issue occurs when a nodal level set value is close to a zero isocurve ($|\bar{s}_i| < h_e 10^{-8}$, where h_e is the element edge length). The problem is here that such a configuration leads to vanishing sensitivities (see Appendix A for details) which must be avoided in order to obtain a numerically stable optimization process. To counter this potential numerical issue, we employ the following simple trick [33]. That is, if a nodal level set value is found to be too close to the zero level, the design variable is set to a fixed value of $\bar{s}_i = h_e 10^{-8}$. This approach increases the stability of the parameterization and results in a negligible perturbation of the level set value in the direction of the solid without effecting the course of optimization.

3. Analysis

3.1. Governing equations

In this section, the governing equations for the structural displacements and the acoustic pressure are introduced. In order to allow the design to evolve in the defined domain Ω, both fields (acoustic pressure and structural displacements) are solved in the entire computational domain ($\Omega = \Omega_s \cup \Omega_a$). The structural response is governed by the time-harmonic elasticity equations (without body forces):

$$\nabla^T \boldsymbol{\sigma} + \omega^2 \rho_s \mathbf{u} = 0 \qquad \text{in} \quad \Omega \tag{3}$$

$$\mathbf{u} = \mathbf{u}_0 \qquad \text{on} \quad \Gamma_{sd} \tag{4}$$

$$\mathbf{n}_s^T \boldsymbol{\sigma} = \mathbf{f} \qquad \text{on} \quad \Gamma_{sn} \tag{5}$$

$$\mathbf{n}_s^T \boldsymbol{\sigma} = p \mathbf{n}_a \qquad \text{on} \quad \Gamma_{as} \tag{6}$$

Here, $\mathbf{u}$ is the displacement vector, $\boldsymbol{\sigma}$ is the Cauchy stress vector defined as $\boldsymbol{\sigma} = \boldsymbol{\mathcal{C}}(E_s, \nu)\,\boldsymbol{\epsilon}$, where $\boldsymbol{\mathcal{C}}$ and $\boldsymbol{\epsilon} = \left[\frac{\partial u_1}{\partial x}, \frac{\partial u_2}{\partial y}, \frac{\partial u_1}{\partial y} + \frac{\partial u_2}{\partial x}\right]^T$ denote the constitutive matrix for plane stress and the strain vector, respectively. The radial frequency is denoted by ω, ρ_s is the density of the solid, E_s is the Young's modulus and ν is the Poisson's ratio. The time-harmonic traction force is given by the amplitude vector $\mathbf{f}$. The normal vector $\mathbf{n}_s$ is defined at the coupling interface Γ_{as} and is directed from the solid domain towards the acoustic domain, likewise $\mathbf{n}_a$ is the normal vector pointing outwards from the acoustic domain.

The Dirichlet and Neumann boundary conditions employed in the system are listed from Eqs. 4 to 6 and are defined at the boundaries Γ_{sd} and Γ_{sn}, respectively. The coupling between acoustic and solid domains is provided through Eq. 6 where the pressure fluctuations in the acoustic domain act as a pressure load to the solid through the interface Γ_{as}. In the fictitious domains (in Ω_a for displacements), void phase is realized by changing the material properties of the solid (section 3.2) to a small number similar to density methods.

The acoustic pressure is governed by the scalar Helmholtz equation:

$$\nabla^T \left(\frac{1}{\rho_a} \nabla p\right) + \left(\frac{\omega^2}{K_a}\right) p = 0 \qquad \text{in } \Omega \tag{7}$$

$$p = p_0 \qquad \text{on } \Gamma_{ad} \tag{8}$$

$$\mathbf{n}_a^T \left(\frac{1}{\rho_a} \nabla p\right) = -\omega^2 \mathbf{n}_s^T \mathbf{u} \qquad \text{on } \Gamma_{as} \tag{9}$$

$$\mathbf{n}_a^T \left(\frac{1}{\rho_a} \nabla p\right) + i \frac{\omega}{\rho_a c_a} p = 2i \frac{\omega}{\rho_a c_a} p_{in} \qquad \text{on } \Gamma_{ar} \tag{10}$$

Here, p is the pressure, $K_a = c_a^2 \rho_a$ is the acoustic bulk modulus where the density and the speed of sound in the acoustic medium are denoted by ρ_a and c_a, respectively. Eq. 10 is the boundary condition on Γ_{ar} describing plane wave radiation with p_{in} denoting the amplitude of an incoming plane wave. The unit complex number is denoted with i. The coupling boundary condition is given in Eq. 9 which represents the coupling to the acceleration of the interface Γ_{as}. The Dirichlet boundary condition for the Helmholtz equation is defined on the boundary Γ_{ad} and given in the Eq. 8. Similarly in the fictitious domains (in Ω_s for acoustic pressure, section 3.2), material properties of a rigid phase are assigned for the solution of the acoustic pressure.

The standard Galerkin procedure is utilized to obtain the weak form of the above described vibroacoustic system, which is written as

$$\int_\Omega \delta\boldsymbol{\epsilon}^T \boldsymbol{\mathcal{C}}\boldsymbol{\epsilon}\ \mathrm{d}\Omega - \omega^2\rho_s \int_\Omega \delta\overline{\mathbf{u}}^T \mathbf{u}\ \mathrm{d}\Omega - \int_{\Gamma_{as}} \delta\overline{\mathbf{u}}^T p\mathbf{n}_a\ \mathrm{d}\Gamma = \int_{\Gamma_{sn}} \delta\overline{\mathbf{u}}^T \mathbf{f}\ \mathrm{d}\Gamma \tag{11}$$

$$\int_\Omega (\nabla\delta\overline{p})^T \frac{1}{\rho_a}\nabla p\ \mathrm{d}\Omega - \omega^2 \int_\Omega \frac{1}{K_a}\delta\overline{p}\ p\ \mathrm{d}\Omega - \omega^2 \int_{\Gamma_{as}} \delta\overline{p}\ \mathbf{n}_a^T \mathbf{u}\ \mathrm{d}\Gamma + i\omega \int_{\Gamma_{ar}} \frac{1}{\rho_a c_a}\delta\overline{p}\ p\ \mathrm{d}\Gamma = 2i\omega \int_{\Gamma_{ar}} \frac{1}{\rho_a c_a}\delta\overline{p}\ p_{in}\ \mathrm{d}\Gamma \tag{12}$$

where, the test functions for the displacements and the pressure are denoted by $\delta\overline{\mathbf{u}}$ and $\delta\overline{p}$, respectively, and $\delta\boldsymbol{\epsilon}$ is the virtual strain. The computational domain is meshed with Q-4 elements and the continuous variables $\mathbf{u}$ and p are approximated at the nodal points by the corresponding isoparametric bilinear shape functions:

$$\mathbf{u} = \mathbf{N}_u\tilde{\mathbf{u}}\,, \qquad \boldsymbol{\epsilon} = \mathbf{B}_u\tilde{\mathbf{u}}\,, \qquad p = \mathbf{N}_p\tilde{p} \tag{13}$$

Here, $\mathbf{B}_u$ denotes the linear strain-displacement matrix. Allowing the test functions to be approximated by the same shape functions as the continuous variables, the discrete form can be written as:

$$\int_\Omega \mathbf{B}_u^T \boldsymbol{\mathcal{C}}\mathbf{B}_u\ \mathrm{d}\Omega\ \tilde{\mathbf{u}} - \omega^2 \int_\Omega \rho_s\mathbf{N}_u^T\mathbf{N}_u\ \mathrm{d}\Omega\ \tilde{\mathbf{u}} - \int_{\Gamma_{as}} \mathbf{N}_u^T\mathbf{n}_a\mathbf{N}_p\ \mathrm{d}\Gamma\ \tilde{p} = \int_{\Gamma_{sn}} \mathbf{N}_u^T\mathbf{f}\ \mathrm{d}\Gamma \tag{14}$$

$$\int_\Omega (\nabla\mathbf{N}_p)^T \frac{1}{\rho_a}\nabla\mathbf{N}_p\ \mathrm{d}\Omega\ \tilde{p} - \omega^2 \int_\Omega \frac{1}{K_a}\mathbf{N}_p^T\ \mathbf{N}_p\ \mathrm{d}\Omega\ \tilde{p} - \omega^2 \int_{\Gamma_{as}} \mathbf{N}_p^T\ \mathbf{n}_a^T\mathbf{N}_u\ \mathrm{d}\Gamma\ \tilde{\mathbf{u}} + i\omega \int_{\Gamma_{ar}} \frac{1}{\rho_a c_a}\mathbf{N}_p^T\ \mathbf{N}_p\ \mathrm{d}\Gamma\ \tilde{p} = 2i\omega \int_{\Gamma_{ar}} \frac{1}{\rho_a c_a}\mathbf{N}_p^T\ p_{in}\ \mathrm{d}\Gamma \tag{15}$$

The discrete approximations are denoted by the superscript tilde as $\tilde{\mathbf{u}}$ and $\tilde{p}$, which is dropped in the remaining of this paper for convenience. The discretized finite element matrices are then identified from the discretized weak form as follows,

The structural system and coupling:

$$\mathbf{K}_s = \int_\Omega \mathbf{B}_u^T\boldsymbol{\mathcal{C}}\mathbf{B}_u\ \mathrm{d}\Omega, \quad \mathbf{M}_s = \int_\Omega \rho_s\mathbf{N}_u^T\mathbf{N}_u\ \mathrm{d}\Omega \tag{16}$$

$$\mathbf{S} = \int_{\Gamma_{as}} \mathbf{N}_u^T\mathbf{n}_a\mathbf{N}_p\ \mathrm{d}\Gamma, \quad \mathbf{f} = \int_{\Gamma_{sn}} \mathbf{N}_u^T\mathbf{f}\ \mathrm{d}\Gamma \tag{17}$$

The acoustic system:

$$\mathbf{K}_a = \int_{\Omega_a} \frac{1}{\rho_a}(\nabla\mathbf{N}_p)^T\nabla\mathbf{N}_p\ \mathrm{d}\Omega \tag{18}$$

$$\mathbf{M}_a = \int_{\Omega_a} \frac{1}{K_a}\mathbf{N}_p^T\mathbf{N}_p\ \mathrm{d}\Omega \tag{19}$$

$$\mathbf{C}_a = \int_{\Gamma_{ar}} \frac{1}{\rho_a c_a}\mathbf{N}_p^T\ \mathbf{N}_p\ \mathrm{d}\Gamma \tag{20}$$

$$\mathbf{g} = 2i\omega \int_{\Gamma_{ar}} \frac{1}{\rho_a c_a}\mathbf{N}_p^T\ p_{in}\ \mathrm{d}\Gamma \tag{21}$$

The system of equations are written:

$$\begin{bmatrix} (\mathbf{K}_s - \omega^2\mathbf{M}_s) & -\mathbf{S} \\ -\omega^2\mathbf{S}^T & (\mathbf{K}_a - \omega^2\mathbf{M}_a + i\omega\mathbf{C}_a) \end{bmatrix} \begin{bmatrix} \mathbf{u} \\ \mathbf{p} \end{bmatrix} = \begin{bmatrix} \mathbf{f} \\ \mathbf{g} \end{bmatrix} \tag{22}$$

Here, the stiffness and the mass matrix of the solid domain are denoted as $\mathbf{K}_s$ and $\mathbf{M}_s$ respectively. Likewise, for the acoustic domain, $\mathbf{K}_a$ is the stiffness matrix and $\mathbf{M}_a$ is the mass matrix. The coupling matrix is denoted as $\mathbf{S}$. The source vectors $\mathbf{f}$ and $\mathbf{g}$ contain the contributions from the boundary conditions.

The present implementation utilizes the PETSc library [46, 47, 48] for its parallel data arrangement and the parallel direct solver MUMPS [49, 50] for the solution of the above discretized system (Eq. 22).

3.2. Implementation aspects of cut element method

To facilitate and ease the notation, an indicator function is defined based on the nodal values of the level set function. The indicator function identifies each element in the computational domain as cut (intersected by the interface) or uncut ($\bar{s} > 0$ or $\bar{s} < 0$ for all nodes). Figure 2 illustrates the identification of cut elements based on the nodal level set values. If an element is not intersected, further marks are assigned which determine if an element belongs to the acoustic ($\bar{s} < 0$ for all nodes) or the solid ($\bar{s} > 0$ for all nodes) region. Different colored elements in figure 2 imply different marks assigned to each element to separate the physical domains.

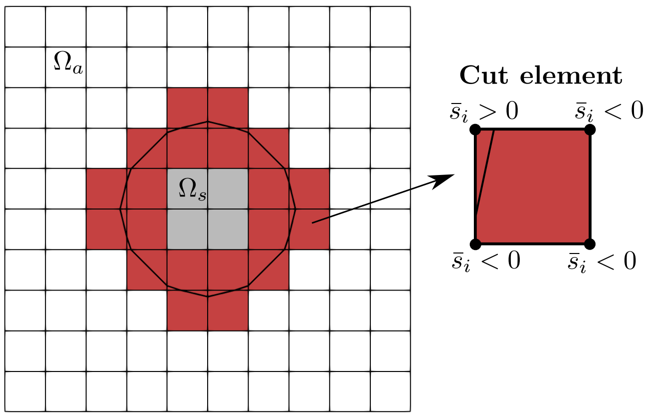

Figure 2: The finite element mesh and the corresponding colors of the elements imply different marks to define the system. The un-cut elements are shown here with white and grey colors. The red color indicates cut elements. An example of one of the conditions to identify the cut elements based on the nodal level set values is also shown. The utilized cut element method provides a linear description of the interface as shown with straight cuts in the illustration.

The integration on un-cut elements is carried out following the usual Gaussian quadrature rule for standard bilinear quadrilateral elements which is written below for the structural stiffness matrix for completeness. Note that the double summation has been replaced by a single summation as this will allow a unified scheme for both cut and un-cut elements.

$$\mathbf{K}_s = \sum_{i=1}^{ng} \mathbf{B}_u^T(\xi_i,\eta_i)\boldsymbol{\mathcal{C}}(E_s,\nu)\mathbf{B}_u(\xi_i,\eta_i)W_i||J(\xi_i,\eta_i)|| \tag{23}$$

Where ng denotes the number of Gauss points, $||J(\xi_i,\eta_i)||$ is the determinant of the Jacobian and W_i is the standard weights for a Q-4 element along with the set of Gauss points $(\xi_i,\eta_i) = (\pm 1/\sqrt{3}, \pm 1/\sqrt{3})$.

The key feature to ensure the accurate modeling of the governing physics is the integration of the cut elements, illustrated by the red color in figure 2. The integration method followed in cut elements is described in section 3.2.1. Finally, it is important to note that all material parameters are spatially dependent. This will be discussed in the model validation example in section 3.3

3.2.1. Integration in cut elements

The core of the cut method is to properly map integration points within a cut element from a sub-triangulation to its parent quadrilateral element, while at the same time keeping track of which face each sub-triangle belongs to. To facilitate the sub-element integration, the intersected element is subdivided into cells with a triangulation algorithm. For this step, based on the nodal level set values we utilize the marching squares algorithm [51] to determine the coordinates of the edges of the intersecting boundary. Afterwards the element is triangulated from a generated look-up table, which constitutes an easy step since the marching squares algorithm describes how a unit cell can be intersected with 6 unique cases and 1 ambiguous case (double-cut configuration). The ambiguity for the triangulation step is resolved by evaluating the level set value at the center of the element. An example of a cut element that is divided into multiple cells can be seen in figure 3(a). After the sub-division, each sub-triangle is assigned an indicator value depending on which phase it belongs to, i.e. marked by either Ω_a or Ω_s as illustrated in figure 3(a). This is easily obtained by inspection of the nodal level set values for the cut element.

The mapping of integration points from a sub-triangles to quadrilaterals is illustrated in figures 3(b)-(c).

The local Gauss points of the triangle $(\boldsymbol{\xi}_T, \boldsymbol{\eta}_T)$ are projected to global coordinates $(\mathbf{x}_G, \mathbf{y}_G)$. The final step is to map $(\mathbf{x}_G, \mathbf{y}_G)$ to the reference quadrilateral c.f. figure 3(c).

$$\xi_{Q,i} = \frac{2\,(x_{G,i} - \min(\mathbf{P}_x))}{(\max(\mathbf{P}_x) - \min(\mathbf{P}_x))} - 1 \tag{24}$$

$$\eta_{Q,i} = \frac{2\,(y_{G,i} - \min(\mathbf{P}_y))}{(\max(\mathbf{P}_y) - \min(\mathbf{P}_y))} - 1 \tag{25}$$

where, $(\mathbf{P}_x, \mathbf{P}_y)$ corresponds to global nodal coordi-

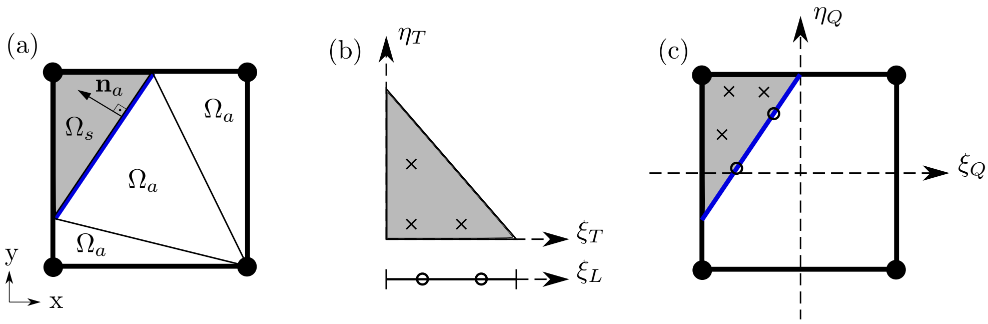

Figure 3: The sub-cell integration (in the structural part) (a) is the triangulated cut element with the corresponding physical domains and the interface indicated with the blue colored line. (b) Iso-parametric linear triangle and line with the corresponding Gauss points are shown in the local coordinates. (c) Illustrates the Gauss points of the triangle and the line which are mapped to the reference domain of the parent element where the sub-integration is carried out.

nates of the quadrilateral element. The integration weights of the sub-triangles are scaled by the area ratio, i.e. $W_{Q,i} = W_{T,i}\left(\frac{4V_T}{V_Q}\right)$ where V_T and V_Q denote the area of the triangle and the quadrilateral, respectively. The factor 4 is the area scaling in local coordinates between a triangular and a quadrilateral element. Noted that the above mapping is only valid for regular quad elements (rectangular) and employed here for simplicity. Otherwise the inverse problem needs to be solved for finding the corresponding local coordinates.

With the mapping complete, the integration can now be carried out following the same rule as stated in equation (23). The only difference is that ng must be replaced by $3nsc$ where nsc is the number of sub-triangles in a cut element. Hence, the same integration is carried out for all elements in the mesh including the fictitious part.

The interface conditions specified at the immersed boundary between acoustic and solid domains are integrated similarly to the area contributions. This can be seen illustrated as the blue line in figure 3(a) and corresponds to mapping the integration points of a one dimensional 2-node linear shape function to the parent quadrilateral. This process is shown in figure 3(b) and (c) and corresponds to letting $W_{Q,i} = W_{L,i}$ and replacing the Jacobian with half the line length, yielding

$$\mathbf{S} = \sum_{i=1}^{ng} \mathbf{N}_u^T(\xi_{Q,i}, \eta_{Q,i})\mathbf{n}_a\mathbf{N}_p(\xi_{Q,i}, \eta_{Q,i})W_{Q,i}\ l/2 \tag{26}$$

where l is the length of the line segment. As with the area integrals, the contributions from the coupling boundary integration go to the dofs of the parent element. Hence, only local operations are needed for the proposed cut element method which makes it highly suitable for parallel computations.

3.3. Modelling validation

This section presents a validation study for the modelling of a coupled vibroacoustic system with the implemented cut element method. The study considers an acoustic duct as shown with the field plot given in Figure 4(a) and a circle shaped elastic body in the middle of the channel (Figure 4(b)). The acoustic domain is considered to be air with the speed of sound and the density taken as c_a = 342 m/s and ρ_a = 1.21 kg/m^3, respectively. The solid domain is defined with the following material properties: $E_s = 6 \times 10^6$ Pa, ρ_s = 1100 kg/m^3 , ν = 0.49. Additionally, the solid domain utilizes structural damping, i.e., $E_{damped} = (1+\eta i)E_s$ where the loss factor is taken to be $\eta = 0.1$. The coupled system is excited by an incoming acoustic signal of P_{in} = 1 Pa with the frequency f = 2 kHz. The open boundary at the outlet is modelled with an absorbing boundary condition and hard-wall condition is utilized for the acoustic pressure on the top and the bottom boundaries of the channel. The structure in this setup is only excited due to the coupling to the acoustic pressure.

The following *fictitious* material properties are assigned for the vibroacoustic system:

Solid domain:

$$K_r = \frac{K_a}{\alpha}, \quad \rho_r = \frac{\rho_a}{\alpha} \tag{27}$$

Acoustic domain:

$$E_v = \alpha E_s, \quad \rho_v = \alpha \rho_s \tag{28}$$

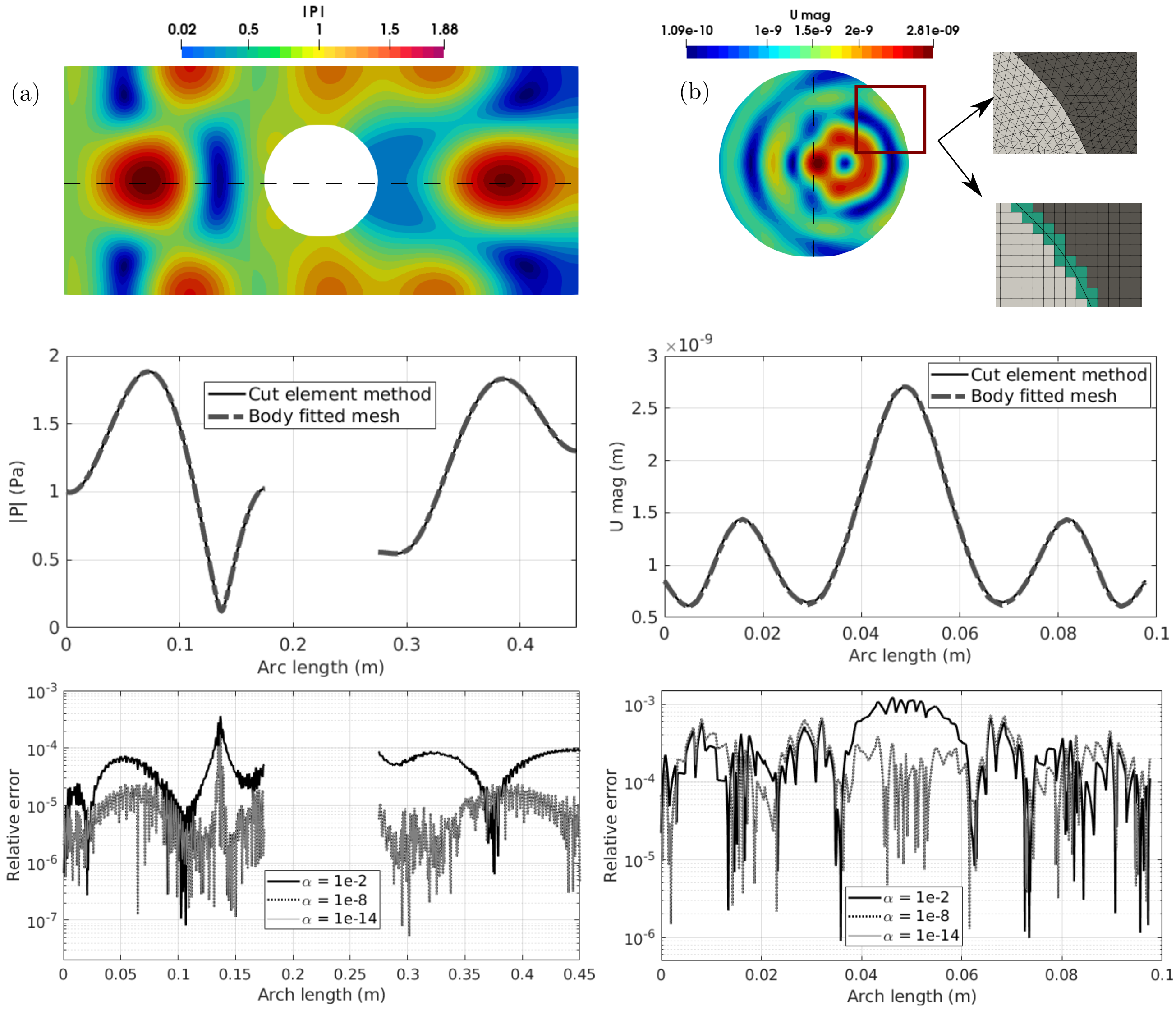

Figure 4: Modelling validation study. (a) Figure showing the absolute pressure field in the considered acoustic duct along with the comparative line plot and the relative error. (b) Figure shows the displacement magnitude field in the structure, the line plot comparing the solution to the COMSOL calculation and the corresponding relative error. The dashed lines in field plots indicate the locations where the cut element solutions are compared to the COMSOL calculations.

where K_r and ρ_r thus represent the acoustic properties of the solid and E_v and ρ_v the elastic properties of the acoustic media. It is important to note that the proposed full domain approach comes at the cost of higher condition numbers for the system matrix compared to that of a segregated analysis. But as shown in Andreasen et.al. [40] for pure solids, the condition numbers are not higher than for density based methods, and hence, do not constitute a numerical problem. The inclusion of a contrast parameter also means that the proposed fictitious domain method avoids the use of e.g. ghost penalties [52] to bound the condition number. This sums to the following requirements for the dimensionless contrast parameter α in Eqs. 27 and 28. The contrast parameter should be chosen small enough not to sacrifice the computational accuracy due to the presence of the fictitious domains, but also large enough to ensure the conditioning of the resulting system is kept at a reasonable level.

Figure 4 compares the cut element solution of the vibroacoustic system to a body-fitted (segregated) solution obtained from the COMSOL Multiphysics software [53]. The field plots of the absolute pressure and the displacement magnitude (realized from the cut element solutions with the dimensionless contrast parameter $\alpha = 10^{-8}$) are shown in Figures 4(a)-(b). The locations of comparisons are highlighted on the field plots with bold dashed lines. The close-up views of the mesh utilized for the study can be seen in 4(b) where the body-fitted mesh is realized with linear triangle elements generated within the COMSOL software and the cut element mesh is composed of regular quad elements. It is clearly seen from the response curves presented in Figures 4(a)-(b) that the present cut element approach successfully captures the acoustic-mechanical interactions and exhibits a very good agreement with the body fitted mesh solutions. Furthermore, we investigate the relative error with respect to the body-fitted mesh solutions with varying the dimensionless contrast parameter α. For high values such as $\alpha = 10^{-2}$ the cut element method exhibits increased errors both in the absolute pressure and the displacement magnitude calculations, but never exceeding a relative error of 10^{-3}. Moreover, lowering the contrast parameter below $\alpha = 10^{-8}$ does not improve the relative error in the solution. This is attributed to the difference in geometry representation and discretizations used in the comparison study. For the remainder of this work, a value of $\alpha = 10^{-8}$ is used as the contrast parameter.

4. Design update - optimization problem

The constrained optimization problem is defined in a general form as the following:

$$\min_{\mathbf{s}} \quad \mathcal{C}(\bar{\mathbf{s}}, \mathbf{v}(\bar{\mathbf{s}})) \tag{29}$$

$$\text{s.t.} \quad \mathbf{r}(\bar{\mathbf{s}}, \mathbf{v}(\bar{\mathbf{s}})) = \mathbf{A}\mathbf{v} - \mathbf{h} = 0 \tag{30}$$

$$g_i \leq 0 \tag{31}$$

$$0 \leq \mathbf{s} \leq 1 \tag{32}$$

Here, $\mathcal{C}$ is the objective function, g_i denotes a set of inequalty constraints, $\mathbf{s}$ is the vector of design variables that are bounded between 0 and 1. The residual vector $\mathbf{r}$ is from the discretization of the coupled linear elastic structure and the acoustic system. Thus, $\mathbf{v}$ is the vector of state variables (displacements and pressure), $\mathbf{A}$ is the discretized system matrix and $\mathbf{h}$ is the source to the system. The design variables $\mathbf{s}$ are updated from the solution of the above optimization problem using the method of moving asymptotes (MMA) algorithm [54] with a parallel PETSc implementation from [55, 56]. The MMA algorithm is utilized with asymptote parameters of 0.5, 0.7 and 1.2 which are the parameters controlling the initial adaptation, decrease and increase of the asymptotes. The MMA penalty parameter for the constraints is set to 1000 and the relative move limit of 0.5% is used. For all examples the optimization procedure is terminated after a fixed number of iterations (determined by numerical experiments) after which the observed design changes experienced are minimal. This choice of stopping criteria is deemed reasonable as all examples presented are of the academic type. We remark that other choices for termination could have been employed, e.g. by requiring the change in physical level set is below a certain threshold [40], i.e. that $||\bar{\mathbf{s}}^{k-1} - \bar{\mathbf{s}}^{k}||_{\infty} < \epsilon$, or by checking the actual convergence of the KKT residual. A detailed description of the sensitivity analysis can been found in Appendix A

5. Optimization of vibroacoustic systems

5.1. Benchmark problem - design of an acoustic partitioner

This example investigates the benchmark problem of designing an optimized elastic structure which acts as a partitioner in an acoustic channel. The example is taken from [57] in order to test the presented formulation on a well studied benchmark problem. The partitioner serves to reduce the transmitted acoustic pressure towards the outlet. The objective of the optimization problem is to minimize the absolute of the acoustic pressure in the downstream region

$$\mathcal{C}(p) = \int_{\Omega_{obj}} |p| \, \mathrm{d}\Omega \tag{33}$$

The illustration of the computational domain along with the boundary conditions are shown in Figure 5, where the coupled system is excited with an incoming pressure signal modeled as a plane wave radiation boundary condition with an input amplitude $P_{in} = 1000$ Pa. The top and bottom walls are considered as hard wall for the acoustic domain and fully clamped for the structural domain. The absorbing boundary condition models an open boundary at the outlet. For the frequency of excitation, $f = 1.0/\pi$ Hz is considered which is considerably lower than the first natural frequency of the system. The optimization problem is subjected to a volume constraint of 65% of the design domain and run for 200 design iterations. The enforcement of a volume constraint lower than the employed percentage created issues of disconnectivity in the thin sections of the structure during optimization iterations. The main reason for this behavior is that the optimization does not consider a length scale. However, it has been found that by increasing the mesh density the optimization can achieve lower volume constraint levels without disconnectivity in the thin sections, this could be attributed to increased design complexity due to finer mesh. The material properties for the structural and the acoustic media are listed in tables 1 and 2. It should be emphasized that the reason to use rather unphysical values for the material properties is to realize identical conditions as found in [57]. In the two forthcoming examples, we will revert to realistic material properties.

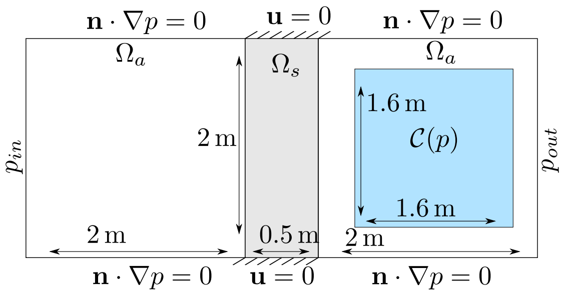

Figure 5: Schematic illustration of example 1 showing the boundary conditions of the optimization problem. Gray color shows the design domain, blue color illustrates the region where the objective function is evaluated.

E [Pa]	ν	ρ_s [Kg/m^3]
1000.0	0.3	15.0

Table 1: Material properties considered for the structure.

Discretization of the computational domain employs a structured mesh with an element size of

c_a [m/s]	ρ_a [Kg/m^3]
1.0	1.0

Table 2: Material properties considered for the acoustic domain.

2×10^{-2} m. A radius of 3 element width is utilized for filtering of the design variables.

With the given computational setup, the considered benchmark problem of designing the acoustic partitioner has previously resulted in a hourglass shape [57] for the elastic structure. In order to achieve this, the optimization problem is solved with several initial configurations and the effect of the initial structure shape on the optimization process is investigated.

The utilized initial designs and the subsequent optimized designs with the individual performance indicators can be seen in Figure 6. The best performing design is demonstrated in Fig. 6(a) which provides approximately 53% better performance than the considered initial guess. The second initial guess Fig. 6(b) considers 5 similarly sized holes placed in the beam and in this case, the performance increase of the end design is reduced to 48.6%. The third and the fourth initial guesses (Fig. 6(c) and 6(d)) are constructed using a cosine function from which the number and the size of the holes can be controlled. The optimized result from Fig. 6(c), although the worst objective function value is obtained, still provides a comparable 45.2% relative performance increase. The initial guess shown at Fig. 6(d) illustrates the effect of increasing the freedom of topological changes during the optimization iterations by starting the optimization with sufficiently high number of holes. Although the end design evolves to a low quality configuration, 68.2% relative increase in the performance is observed. Here it is noted that, although the optimizations (Fig. 6(a) to Fig. 6(c)) reach identical topologies (one hole in the middle of the structure) the shape of the end designs differs significantly. This behavior signifies the strong dependency on the initial guess for the optimization procedure as well as the sensitivity of the problem to shape changes at the interface. It is also worth noting that the optimized design in Figure 6(d) contains a free flying solid inclusion. This should generally be avoided, and can for example be alleviated by adding a constraint as a lower bound of the first eigenfrequency for the structural component or by a constraint on the thermal compliance of the structure when heating with a body force [58].

The sound pressure level (SPL) contours of the initial guess and the optimized design are shown in Fig. 7. The lower sound pressure level towards the outlet is clearly visible for the optimized design. This is achieved due to the response of the

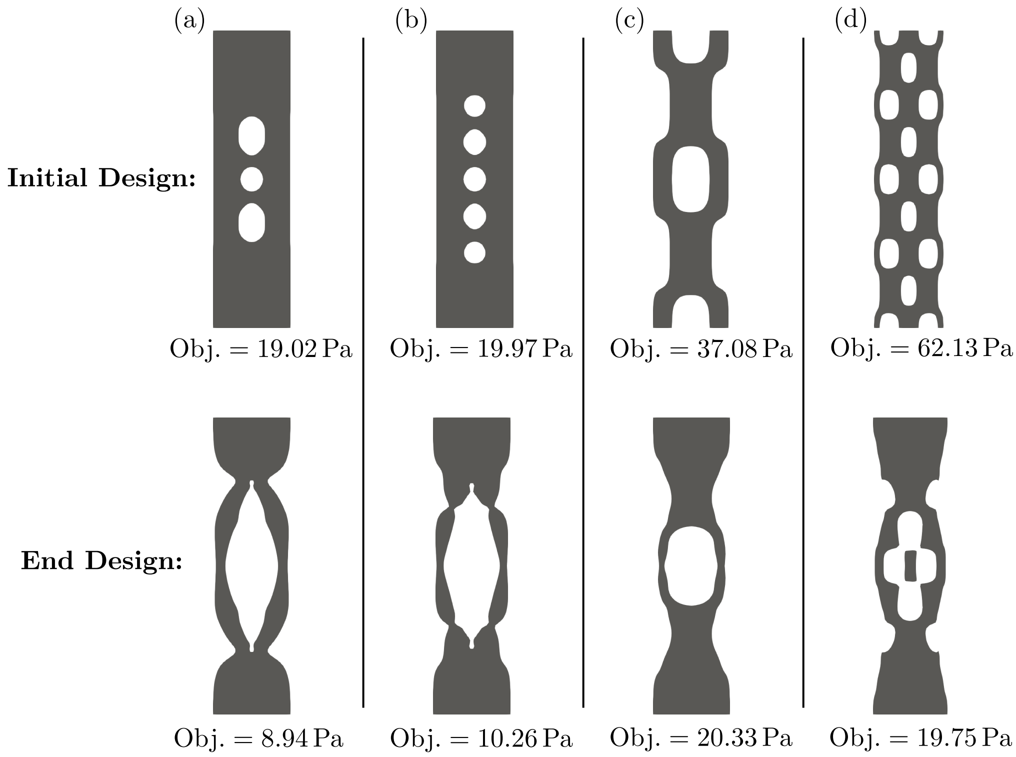

Figure 6: Illustration of the effect of different initial configurations on the optimized design. The first row of figure shows the different initial designs considered for the optimization problem with their calculated objective values (scaled with objective area) and the second row are the subsequent end designs.

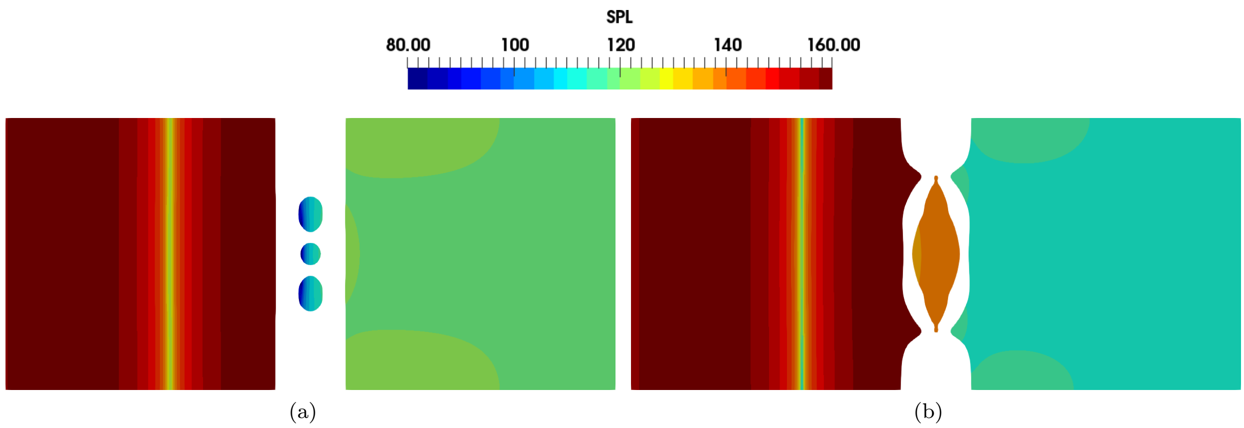

Figure 7: Sound pressure level [dB] contours showing: (a) initial configuration, (b) optimized design.

optimized structure which exhibits vibrations that are greatly reduced in the right arm in comparison to the vibrations in the "inlet" arm of the structure (see figure 8). In this way the transmission of the acoustic waves towards the outlet of the channel is also reduced.

The objective function is evaluated for a range of frequencies and the corresponding response is plotted in Fig. 9(a). Optimization clearly results in the minimization of the response at the optimization frequency and reduced acoustic pressure at the objective area until approximately 0.85 Hz.

Fig. 9(b) shows the iteration history for the objective function (normalized by its initial value) and the volume constraint. Subsequent to the volume constraint being satisfied, in the range of iteration

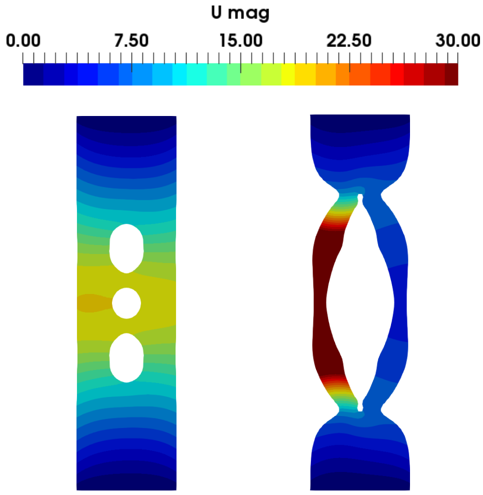

(a) (b)

Figure 8: Displacement magnitude $|\mathbf{u}|$ [m] contours showing: (a) initial configuration, (b) optimized design.

numbers from 90 to 120, the structure undergoes a noticeable change in shape, after which only small local perturbations occurs.

5.2. Bidirectional wave splitter

This example utilizes the developed framework for the design of a bidirectional wave splitter which is considered to be more challenging than the benchmark problem considered in the first example. The boundary conditions along with the computational domain are illustrated in figure 10. The model consists of a dome shaped acoustic domain which is sufficiently large to accommodate outgoing acoustic waves and a structure which has a roller boundary condition applied to the bottom and is excited by a horizontal traction force. Bidirectional wave splitters are used to create directivity of the acoustic waves that are emitted from a vibrating structure based on the frequency of excitation.

The optimization problem considers two equally sized windows to tailor the acoustic waves which are marked as Γ_1 and Γ_2 in the case description (Fig. 10). The objective of the optimization problem is the ratio of the absolute of the acoustic pressure and written for the considered two frequencies as:

$$\mathcal{C}_1(\omega_1) = \frac{\int_{\Gamma_2} |p| \mathrm{d}\,\Gamma}{\int_{\Gamma_1} |p| \mathrm{d}\Gamma}, \qquad \mathcal{C}_2(\omega_2) = \frac{\int_{\Gamma_1} |p| \mathrm{d}\,\Gamma}{\int_{\Gamma_2} |p| \mathrm{d}\Gamma} \tag{34}$$

Here, $\mathcal{C}_1$ with the frequency of excitation ω_1 corresponds to minimizing the absolute pressure of the acoustic waves at the window Γ_2 and maximizing at the window Γ_1 whereas $\mathcal{C}_2$ considers the opposite for the second excitation frequency ω_2. In order to realize an optimization problem with equally minimized multiple objective functions, we cast the problem in a min-max formulation where the optimization considers the minimization of the maximum of the utilized objective functions.

$$\min_{\mathbf{s}} \max \quad [\mathcal{C}_{\Gamma_1}(\omega_1), \mathcal{C}_{\Gamma_2}(\omega_2)] \tag{35}$$

$$\begin{aligned} \text{s.t.} \quad & \mathbf{r}(\bar{\mathbf{s}}, \mathbf{v}(\bar{\mathbf{s}})) = \mathbf{A}\mathbf{v} - \mathbf{h} = 0 \\ & 0 \le \mathbf{s} \le 1 \end{aligned} \tag{36}$$

As written above, the problem is not differentiable. Thus, it is solved using the following bound formulation [59]:

$$\min_{\mathbf{s},\,\beta} \quad \beta \tag{37}$$

$$\text{s.t.} \quad \mathbf{r}(\bar{\mathbf{s}}, \mathbf{v}(\bar{\mathbf{s}})) = \mathbf{A}\mathbf{v} - \mathbf{h} = 0$$

$$\mathcal{C}_{\Gamma_1}(\omega_1) < \beta \tag{38}$$

$$\mathcal{C}_{\Gamma_2}(\omega_2) < \beta \tag{39}$$

$$0 \le \mathbf{s} \le 1 \tag{40}$$

Here, an additional variable β is introduced as the upper bound. Instead of dealing with a multi objective function, the formulation only considers the minimization of this upper bound while defining the objective functions in Eq. 34 as constraints. Since filling the design domain only with solid does not form a trivial answer, the optimization problem does not utilize a volume constraint on the structure.

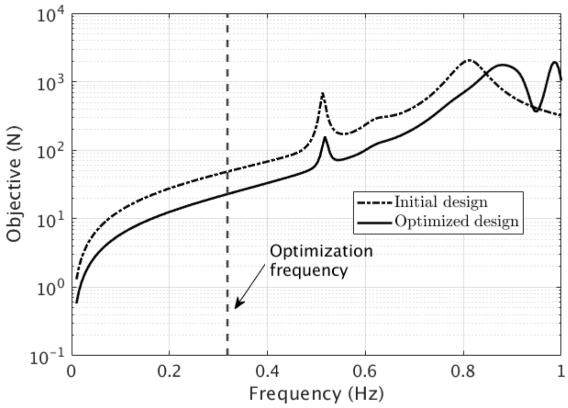

(a)

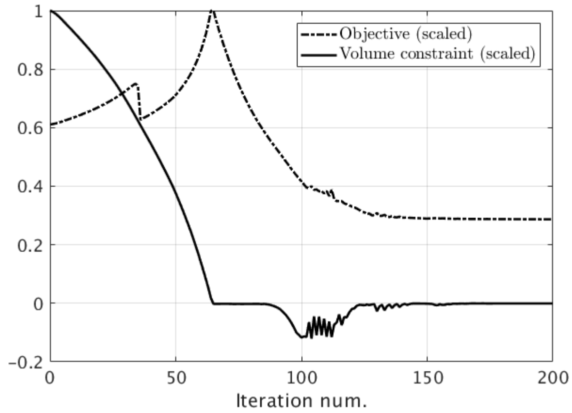

(b)

Figure 9: (a) Frequency response of the objective function comparing the optimized design and the initial configuration, (b) the iteration history of the objective function and the volume constraint.

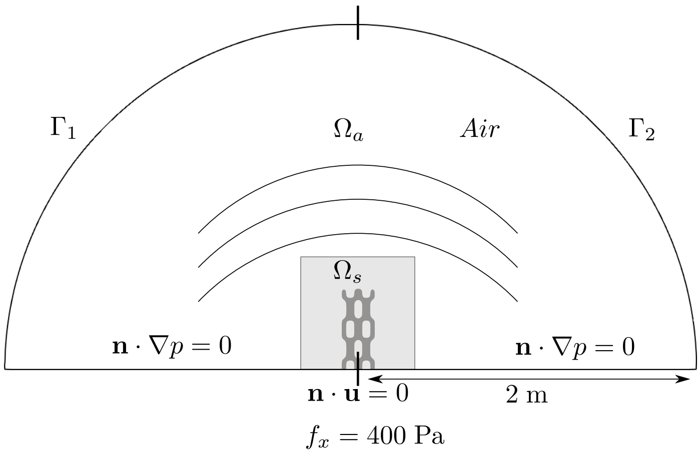

Figure 10: Schematic illustration showing the boundary conditions of the optimization problem. Light gray color shows the design domain whereas the darker gray is the initial design configuration. The outlet section is divided into two equal size subsections marked as Γ_1 and Γ_2 which illustrates the locations where the objective function is evaluated and the acoustic waves are focused.

E [Pa]	ν	ρ_s [Kg/m^3]	η
1×10^9	0.45	1100.0	0.1

Table 3: Material properties considered for the structure.

c_a [m/s]	ρ_a [Kg/m^3]
342.0	1.21

Table 4: Material properties considered for the acoustic domain.

The considered material properties for the structure are listed in table 3 where the loss factor η denotes the amount of structural damping ($E_{\text{damped}} = (1 + \eta\, i)E$) utilized in the structure.

For the acoustic domain, air is considered as the material and the corresponding acoustic properties of air are written in table 4. The computational domain is discretized with a structured mesh having an approximate element size of 1.0×10^{-2}m. The design domain (enclosed rectangular area, Fig. 10) utilizes a regular grid whereas the rest of the domain employs mapped quad elements. Overall, the computational mesh consists of $43,000$ elements.

The initial configuration of the structure, with which the optimization procedure is started, can be

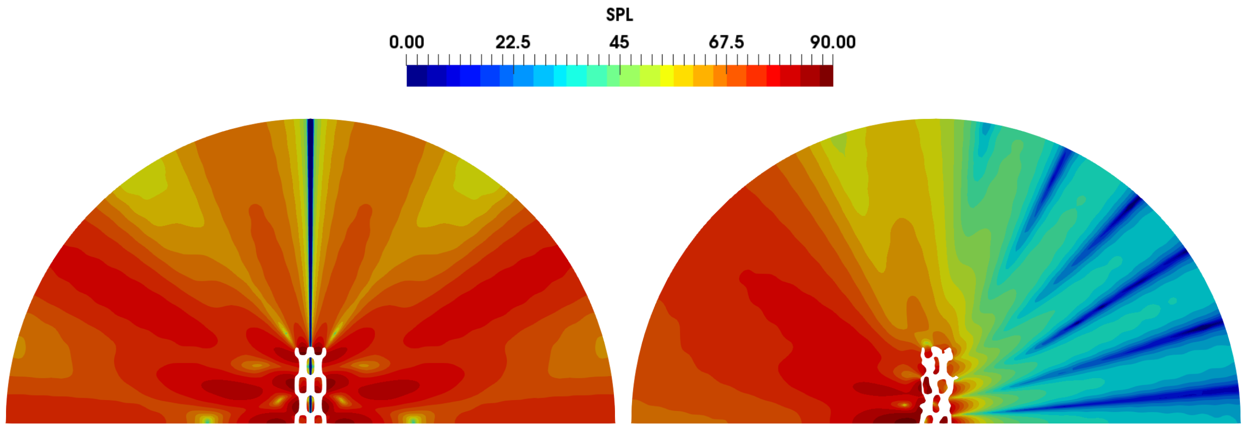

(a) Initial design and the resulted SPL contour for the frequency 1.15 kHz. The objective value of the initial design, $\mathcal{C}_1 = 1.0$.

(b) The optimized design showing the SPL contour for the excitation frequency 1.15 kHz. The objective value of the end design, $\mathcal{C}_1 = 0.02129$.

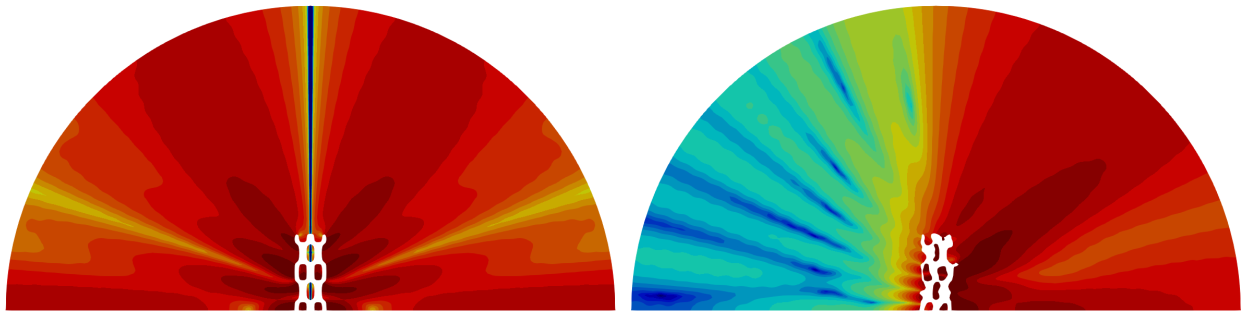

(c) Initial design and the resulted SPL contour for the frequency 1.50 kHz. The objective value of the initial design, $\mathcal{C}_2 = 1.0$

(d) The optimized design showing the SPL contour for the excitation frequency 1.50 kHz. The objective value of the end design, $\mathcal{C}_2 = 0.02130$.

Figure 11: Sound pressure level [dB] contours plotted for both optimization frequencies, comparing the initial design configuration and the optimized design.

seen in figure 10 where it is illustrated with a darker gray color in the design domain. The initial guess is realized with the use of a cosine function which allows to form a predefined number of holes in the initial structure. The optimization utilizes a filter width of 1 element. Two discrete frequencies of excitation, i.e., 1.15 kHz and 1.50 kHz are considered to tailor the acoustic waves and the optimization is run for 600 design iterations.

The resulting optimized design for a bidirectional wave splitter can be seen from figure 11. The plots are colored with SPL contours which compare the initial guess and the optimized design for the two considered excitation frequencies. The optimized design clearly achieves a directivity for the emitted acoustic waves. For the first considered excitation frequency 1.15 kHz the acoustic waves are focused towards the left side of the dome, effectively minimizing the acoustic pressure at the targeted window Γ_2. Shifting the excitation frequency to 1.50 kHz creates the opposite effect and acoustic waves are focused towards the right side of the dome. Due to the interaction between the vibrating structure and the surrounding air, a cancellation effect for the acoustic waves occur towards the targeted windows and strong outgoing waves are formed towards the opposite sides of the dome. This behavior creates a division in the direction of the emitted waves which can be controlled with varying the operating frequency as illustrated in figures 11(b) and 11(d).

The objective values of the end design calculated for the two considered excitation frequencies, $\mathcal{C}_1$ and $\mathcal{C}_2$ are very close to each other and the optimized design realizes a 98% performance increase when compared to the initial configuration.

Figure 12 plots the absolute pressure level at the

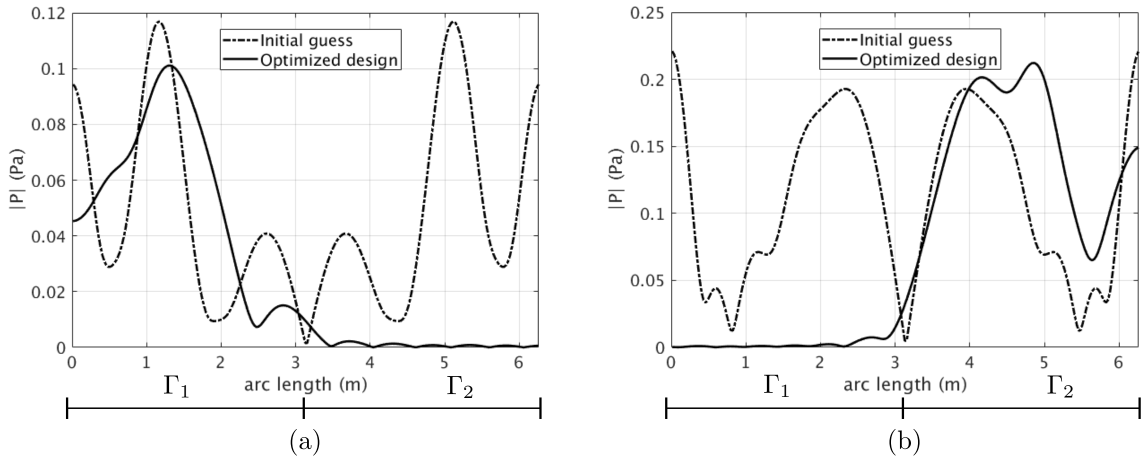

Figure 12: Absolute pressure values from the outer dome of the computational domain, (a) the excitation frequency 1.15 kHz, (b) the excitation frequency 1.50 kHz.

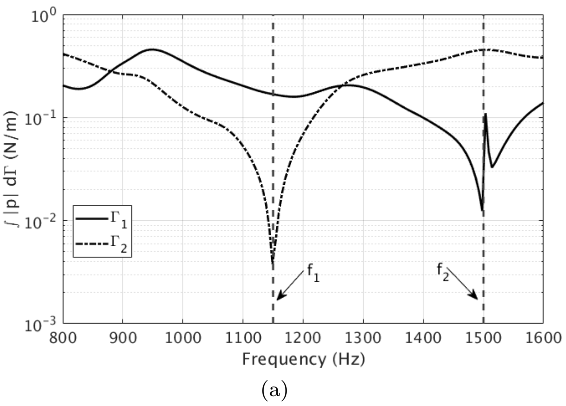

Figure 13: Frequency response of absolute of the acoustic pressure integrated at the two windows Γ_1 and Γ_2.

outlet of the computational domain where the directivity of the acoustic waves based on the excitation frequency is shown. As it can be seen from the figure, the acoustic waves are symmetrically emitted by the initial structure, since the initial shape of the vibrating structure has a vertical symmetry. In the focused windows, the pressure of the acoustic waves has a comparable magnitude to the response of the initial configuration. Since it is not possible to create a 1 - 0 discrete switch for the acoustic waves with the current setup, the response of the optimized design exhibits small variations of the acoustic pressure in the windows that are targeted to be minimized for the considered frequencies. Furthermore, the frequency response of the absolute pressure integrated across the two windows Γ_1 and Γ_2 is plotted in figure 13 and shows that the behaviour is localized to the optimization frequencies ($f_1 = 1.15\,\text{kHz}$, $f_2 = 1.50\,\text{kHz}$) resulting in sharp dips in the frequency response near these frequencies. Overall the design for the bidirectional wave splitter performs effectively.

Figure 14 illustrates the deformations in the optimized structure which result in the directivity of the outgoing acoustic waves. Figure 14(a) shows the undeformed state from which it can be seen that the optimization does in fact not change the topology of the initial configuration and keeps the initial number of holes. Instead, it is sufficient to alter the shape of the structure to tailor the emitted acoustic waves. Furthermore, the physical level set field $\bar{\mathbf{s}}$ of the optimized design is shown in figure 15, which we note is representative for the examples studied here. From this figure, one can see that the spatial gradient of the level set field does not become flat, and hence that the upper bound for the gradient is sufficient to ensure a robust and stable design procedure for the problems investigated in this work.

The structure exhibits large amplitude vibrations on the left middle section (Fig. 14(b)) with the excitation frequency 1.15 kHz and the vibrations on the left side of the optimized design are the main contributor to form the outgoing waves which are focused towards the window Γ_1. The vibrations of the right side of the optimized design generate acoustic waves that mainly cancel out. The second optimization frequency 1.5 kHz results in a response that is shown in figure 14(c) where the interaction between the vibrating structure and the acoustic

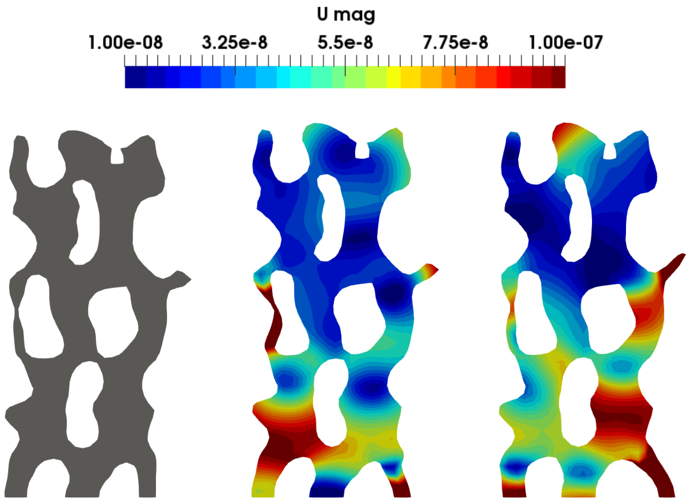

(a) (b) (c)

Figure 14: The optimized design where the deformed structures are colored with displacement magnitude $|\mathbf{u}|$ [m] , (a) undeformed structure, (b) deformed structure vibrating with the excitation frequency 1.15 kHz, (c) deformed structure vibrating with the excitation frequency 1.50 kHz.

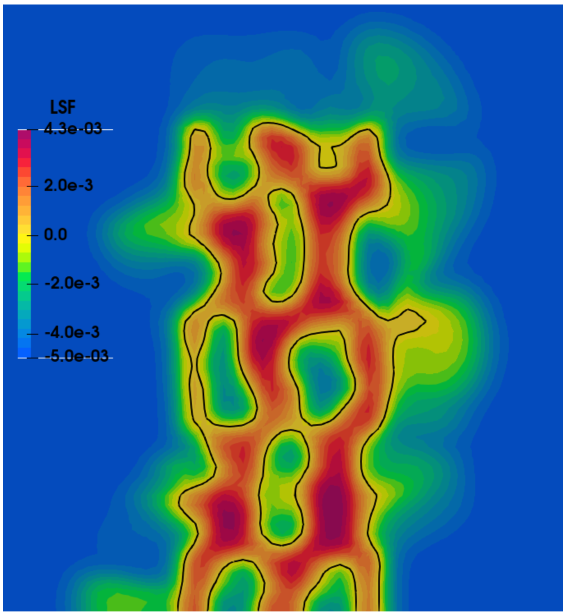

(a)

Figure 15: The physical level set field $\bar{\mathsf{s}}$ where the zero level contour is highlighted to illustrate the resulted optimized design.

domain successfully focuses the emitted waves towards the window Γ_2.

Overall, it is noted that the final topology is directly dictated by the initial design as was also seen in the first example in section 5.1. However, it is also noteworthy that only modifying the shape allows for a significant change of the system behavior as it is illustrated in this section with the design of a bidirectional wave splitter. This justifies the use of advanced shape optimization methods, such as the explicit level set method, for tailoring the vibroacoustic response of a complex system, which will be further exploited in the final example.

5.3. 2D model of a hearing aid suspension system

The final example studies the use of the presented method to a more application oriented optimization case which concerns the feedback problem of a hearing aid using a simplified model. The feedback issues can occur through various ways in a hearing aid and are experienced when the hearing aid microphone picks up unwanted sound and vibrations from various sources. One contributor to feedback is vibrations of the hearing instrument due to high acoustic pressure levels. The vibrations are converted to a microphone signal that may result in a negative feedback loop.

A simplified 2D model of a hearing aid is illustrated in Fig. 16 where the model consists of two bodies connected by a suspension structure. The rest of the model contains an internal air channel along with an acoustic cavity for the optimization case A (Fig. 16(a)) and open boundaries which is modeled with an absorbing boundary condition for the optimization case B (Fig. 16(b)). The consid-

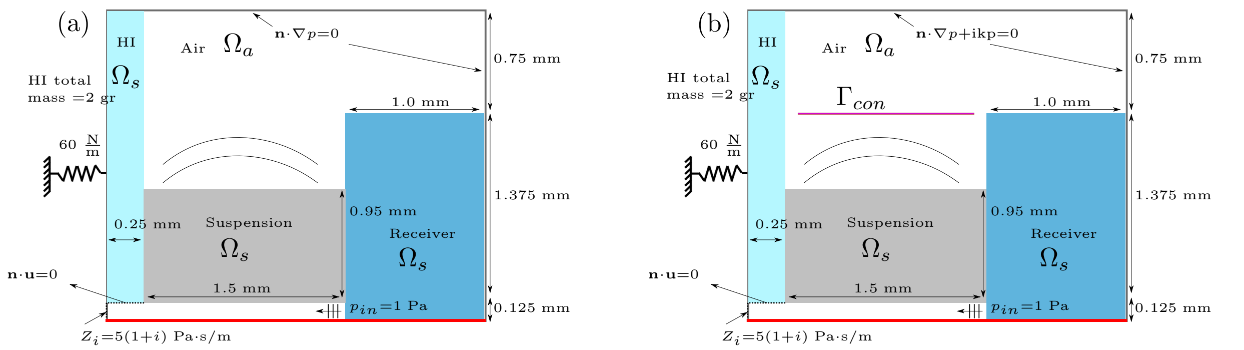

Figure 16: Schematic illustration of the optimization problem including the boundary conditions applied. Gray color shows the design domain, light blue color is the region where the objective function is evaluated. The darker blue indicates the receiver structure, the red color shows the symmetry line. (a) The optimization setup A, top and the back of the domain is hard wall, (b) the optimization setup B where the top and the back of the domain is changed to absorbing b.c. and purple color is the line where the constraint function is evaluated.

ered system is excited by an acoustic signal generated by the receiver (loudspeaker).

In a more complex setting, the internal channel represents a tube that guides the sound produced from the receiver into the ear canal. The current model lacks the complexity of the tube and the internal channel is cut-off, the resistance to the incoming acoustic wave is taken into account with the utilized specific impedance at the end of the channel. The hearing instrument (HI) signifies the rest of the mechanical components that surround the internal channel, which in the current simplified model is considered as an added mass to the system. The density of the HI is calculated such that the specified mass is derived and the rest of the material properties are assigned to realize a near rigid body behavior. The bottom of the HI is constrained in the vertical direction to avoid unrealistic vibration modes.

The purpose of the suspension structure, apart from structural support, is to reduce the structural vibrations caused by the acoustic wave coming from the receiver. The shape of the suspension structure is allowed to change in order to decrease the vibrations at the HI. The receiver and HI are not included in the optimization domain hence their initial shapes do not change throughout the optimization process.

	E [Pa]	ν	ρ_s [Kg/m^3]	η
Suspension	6×10^6	0.49	1100.0	0.1
Receiver	2×10^{11}	0.3	2.2×10^4	0

Table 5: Material properties considered for the structure.

In a general sense the volume of the suspension system does not have an importance for the performance of the device, hence the optimization problem does not utilize a volume constraint. The objective function is the total vibration of the body that represent the HI and written as:

$$\mathcal{C}(\mathbf{u}) = \int_{\Omega_s} |\mathbf{u}| \, \mathrm{d}\Omega \tag{41}$$

The material properties of the suspension and the receiver structures are listed in table 5 and the utilized acoustic properties of air are listed in table 4. Structural damping is considered for the suspension structure and modeled as an imaginary part of the Young's modulus $E_{\text{damped}} = (1 + \eta\, i)E$, where η is the loss factor.

For the discretization of the computational domain illustrated in figure 16, a structured mesh with an element size of 1.25×10^{-5}m is utilized. As a starting point to the analysis and optimization of the suspension system, a benchmark design of a simple, yet relevant rectangular shape is considered. In a realistic 3D setting, the benchmark design would correspond to a hollow cylinder around the internal channel. The initial guess (Fig. 17(b)) to the optimization procedure is formed with 3 equally spaced semicircles on the top surface of a rectangular shape which increases the surface area of the initial configuration to provide more freedom for design change. The optimization is carried out for 5 discrete frequencies, i.e., 5 kHz, 5.5 kHz, 6 kHz, 6.5 kHz and 7 kHz and run for 250 design iterations. The objective function is evaluated and summed together with equal weights at each considered frequency. In order to have smooth bound-

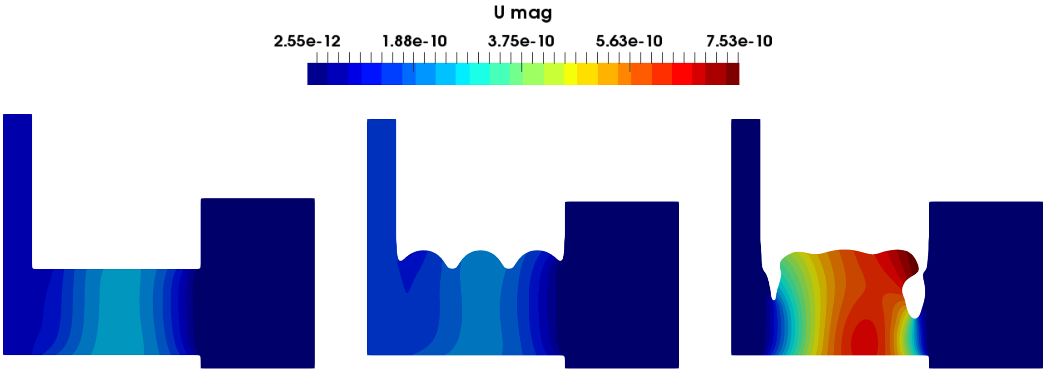

(a) (b) (c)

Figure 17: The optimization case A: displacement magnitude $|\mathbf{u}|$ [m] contours for the frequency 7 kHz showing: (a) benchmark design, (b) initial guess for the optimization, (c) optimized design.

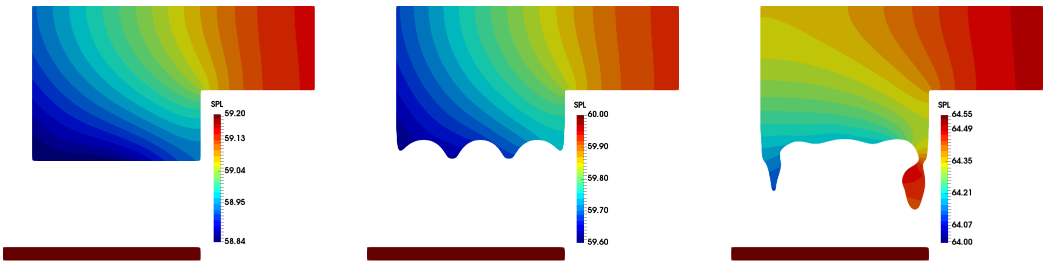

(a) (b) (c)

Figure 18: The optimization case A: sound pressure level [dB] contour for the frequency 7 kHz. (a) benchmark design, (b) initial guess for the optimization, (c) optimized design.

aries throughout the iteration history in the design domain, the optimization utilizes a filter radius of 4 elements, which is chosen since extensive numerical experiments have shown this to be the best performing for the considered case.

The results of optimization case A which does not consider a constraint on the optimization problem can be seen in figure 17. The figure compares three structures, namely the benchmark, initial guess and the optimized design of the suspension structure along with the receiver and HI body which are colored with the displacement magnitude contour. From the visual inspection of the displacement contours (Fig. 17), which is plotted for a single frequency of 7 kHz, the HI body clearly exhibits a noticeable reduction in the vibration level with the optimized shape of the suspension design. However, it is also seen that the reduced vibration level of the HI is accompanied by an increased vibration level at the suspension structure. The benchmark design and initial guess exhibit similar behavior in terms of the plotted displacements.

Figure 18 shows the sound pressure level (SPL) for a single frequency of 7 kHz in the acoustic domain comparing both initial and optimized design configurations along with the benchmark design. From the contour lines it is seen that due to the reduced vibrations, the HI body has an effect similar to a hard wall (Fig. 18(b)) and the SPL contours plotted for the benchmark design and initial guess are very comparable. Here it is noted that, the optimized design exhibits approximately 5 dB higher SPL in the acoustic cavity above the suspension structure due to the increased vibration level of this part.

The optimization case B (Fig. 16(b)) investigates the effect of controlling the allowable acoustic power that is emitted from the vibrating suspension structure. The main reason for studying this case is that, the previously optimized design has a significantly higher vibration level (Fig. 17(c)) at the suspension structure, which causes generation of high sound pressure levels (5 dB increase for 7 kHz as shown in Fig. 18(c)) towards the back of the hearing aid. Hence, in addition to the objective function Eq. 41, the time-averaged transported

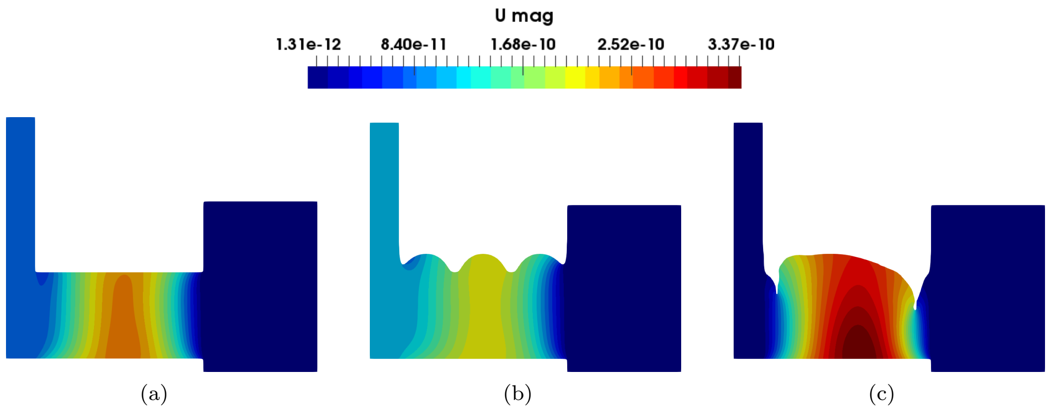

Figure 19: The optimization case B: displacement magnitude $|\mathbf{u}|$ [m] contours for the frequency 7 kHz showing: (a) benchmark design, (b) initial guess for the optimization, (c) optimized design.

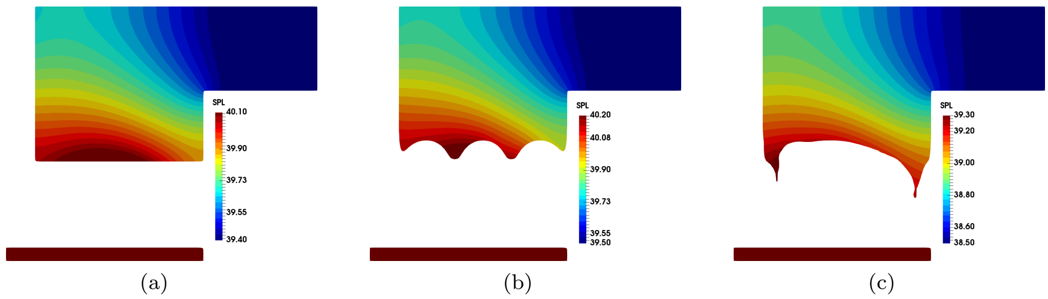

Figure 20: The optimization case B: sound pressure level [dB] contour for the frequency 7 kHz. (a) benchmark design, (b) initial guess for the optimization, (c) optimized design.

power (intensity) through the specified line (shown in the figure 16(b)) above the suspension structure is controlled using a reference transported power. Here it is noted that, in order to have a power transportation in a time-averaged sense, the hard wall boundary conditions of the top and the back of the computational domain are changed to absorbing boundary condition for this example (Fig. 16(b)).

The normal component of the intensity is given as [60]:

$$\mathcal{J} = \frac{1}{2\rho_a \omega} \int_{\Gamma_{con}} \Re \left(-i\, p \left(\mathbf{n}_a^T\ \nabla \overline{p} \right) \right)\ \mathrm{d}\Gamma \tag{42}$$

Here, $\overline{p}$ is the complex conjugate of the pressure variable and i is the complex unit. The constraint function for the transported power is then written as

$$g(p) = \sum_{\omega=\omega_1}^{\omega_n} \frac{\mathcal{J}(\omega)}{\beta\, \mathcal{J}_{ref}} - 1 \leq 0 \tag{43}$$

Where $\mathcal{J}_{ref}$ is the reference power value and calculated as the sum of the transported power evaluated from the initial guess for all considered frequencies. The parameter β controls the level of the allowed power in the design and is set to $\beta = 1$ for the optimization. That is, the optimized design can only emit as much power as the initial guess through the specified line in the domain. The considered constraint is a function of a state variable. Hence an additional adjoint equation is solved for each optimization frequency during design iterations in order to calculate the required gradients of the constraint function.

The optimized structure for case B can be seen from figure 19 where it is compared to the initial configuration and the benchmark design. The plot is colored with displacement magnitude. Even though the current problem includes an additional constraint on the transported power, the vibrations at HI mass are still effectively reduced with the optimized shape of the suspension structure. The optimized design has a similiar response to the one obtained with the optimization case A. In order to reduce the vibrations at the HI mass, the structure

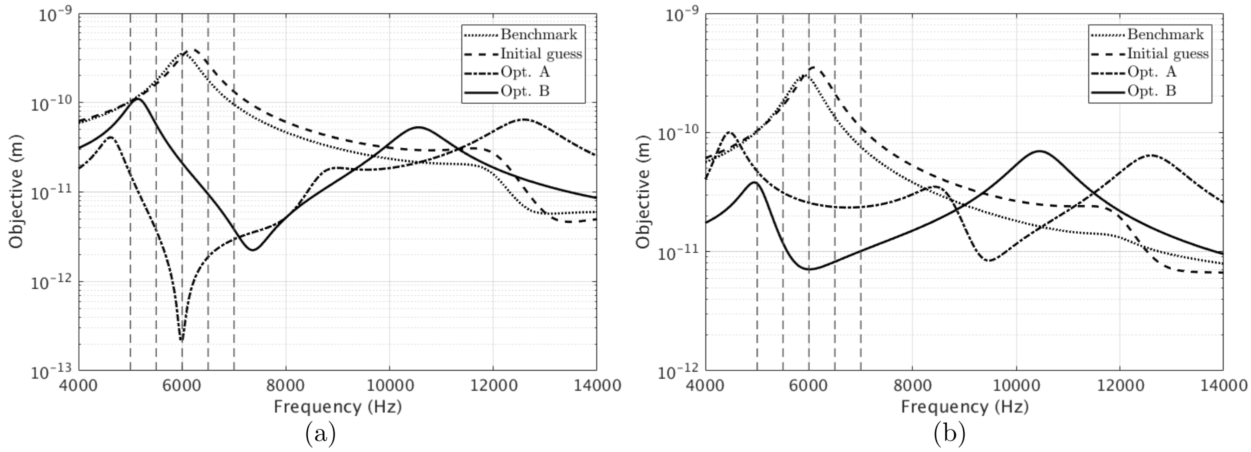

Figure 21: Frequency response of the objective function (scaled with the objective area), vertical dashed lines are the discrete frequencies of optimization, (a) response of case A (hard walls), (b) response corresponding to case B (absorbing BC's).

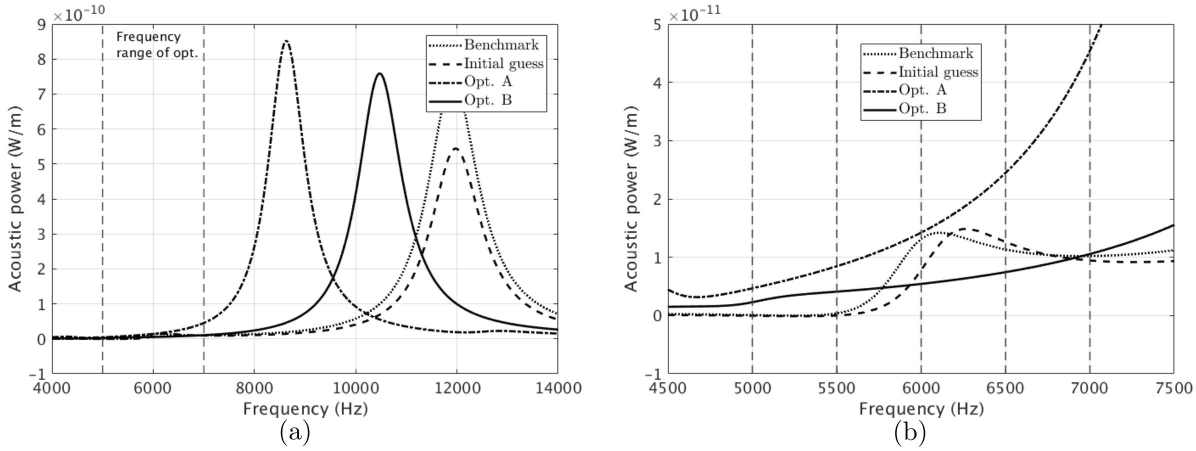

Figure 22: Frequency response of the acoustic power integrated at the line Γ_{con}, vertical dashed lines are the discrete frequencies of optimization, (a) full frequency sweep, (b) frequency range of optimization.

vibrates more at the suspension. However, for optimization case B, the vibrations are reduced to satisfy the constraint on the emitted acoustic power.

Figure 20 shows the sound pressure levels in the acoustic domain for optimization case B. A visual inspection reveals that the optimized design exhibits slighty lower pressure levels towards the back of the hearing aid and the SPL contours of both structure (initial guess and benchmark) along with the optimized design are indeed similar.

The optimized designs obtained from cases A and B are investigated with a frequency response of the objective function in figure 21. The frequency responses evaluate and compare the obtained designs with each other along with the initial guess utilized for the optimizations and the benchmark design. From figure 21 it can be seen that both optimized designs perform best for their own analysis types, which validates the optimization results for the purpose of a crosscheck study. In figure 21(a) (from optimization case A) the optimization effectively results in the minimization of the resonance around 6 kHz and the optimized suspension structure performs very well. In case B (Fig. 21(b)), the optimized design also shifts the response curve such that the resonance around 6 kHz is effectively minimized. For their respective boundary condition setups, the optimized design from case A exhibits reduced vibrations until approximately 11 kHz whereas optimization case B results in a reduction of the vibrations at HI mass until around 9 kHz. When the optimized design from case B is run with setup A and vice versa, it is seen that the designs perform differently. Still the reduction in vibrations at HI mass is apparent for both designs even under conditions that they are not optimized for. The benchmark design and the utilized initial guess perform very close for the considered range of frequencies and the considered boundary condition setups do not create significant change in the behavior for these structures.

Figure 22(a) plots the acoustic power and the frequency range of optimization is zoomed for better inspection (Fig. 22(b)). The constraint function, which is utilized in the optimization case B, is satisfied at the final design and it can be seen that, in average, the optimized design emits the same level of acoustic power for the considered frequencies. As expected, the initial guess and the benchmark design emit very comparable levels of acoustic power. The optimized design from case A produces significantly higher acoustic power in the frequency range of optimization. In a more complex setting of a hearing aid, this could cause problems of high pressure levels inside the device. The optimization from case B also minimizes the resonance around 12 kHz by shifting it towards lower frequencies and tailoring the response to satisfy the constraint on the acoustic power in the optimization frequencies. The peak of the shifted resonance is still at a frequency higher than 10 kHz. With the optimized design from case A however, the peak of the resonance is shifted to approximately 8.5 kHz which results in the increased acoustic power in the considered range.

6. Conclusions

The article demonstrates the application of an explicit level set based generalized shape optimization method within the discrete adjoint approach for time-harmonic coupled acoustic-structural systems. The shape optimization is facilitated on a fixed mesh using an immersed boundary cut element method. The method allows for modelling complex geometries accurately without the costly operation of re-meshing the interface, instead of which an integration scheme is carried out on cut elements. Thus, the methodology does not change the DOF number of the system and is easily accommodated in an existing parallel FEM code structure. Straightforward inclusion of multiple constraints and different optimization formulations such as min-max problems are achieved by linking the proposed nodal level set description to the mathematical design variables and utilizing the method of moving asymptotes (MMA) algorithm for the design updates. An initial guess study is provided which considers a benchmark problem of the design of an acoustic partitioner. Here, hour glass shaped designs are achieved as previously observed in the literature [13, 57]. The example also demonstrates the sensitivity of the coupled vibroacoustic problem to shape changes at the interface with a performance that differs significantly for similar topologies with different shapes. The shape optimization for a bidirectional wave splitter is carried out resulting in a remarkable directivity of the emitted acoustic waves at two discrete frequencies. The resulting optimized design does not change the initial number of holes in the structure and the system behavior is significantly improved only with shape changes justifying the use of the proposed shape optimization method for tailoring the vibroacoustic response of complex systems. Finally, an application oriented optimization case is considered to improve the performance of a simplified 2D model of a hearing instrument. The shape of the suspension structure around the internal channel is optimized to reduce the structural vibrations caused by an incoming acoustic signal generated by the receiver. The example also demonstrates how constraining the acoustic intensity can be used to control the vibration levels in the optimized suspension structure. The presented designs effectively reduce the structural vibrations in the simplified hearing instrument model.

Future research will focus on combining density based topology optimization for the generation of good quality initial designs and on the extension to 3D to demonstrate the applicability of the methodology on industrial problems. Also, it should be noted that hexahedral elements are prone to more ambiguities when cuts are introduced than that seen for the quadrilaterals. However, this can be fully alleviated if using tetrahedral elements or, as done in this work, by systematic testing of the phase of the interior points.

7. Acknowledgements

The authors wish to thank Ester Creixell-Mediante from Oticon for discussions regarding hearing aid systems and for providing data for the 2D simplified hearing aid model.

Appendix A. Sensitivity analysis

In order to carry out the optimization process with a gradient-based optimizer algorithm, the sensitivity information of the objective function and the constraints are needed. In this work, the discrete adjoint method is utilized for the calculation of sensitivities.

Firstly, the objective function $\mathcal{C}$ is augmented with a set of Lagrange multipliers

$$\mathcal{L} = \mathcal{C}(\bar{\mathbf{s}}, \mathbf{v}(\bar{\mathbf{s}})) + \boldsymbol{\lambda}^T \mathbf{r}(\bar{\mathbf{s}}, \mathbf{v}(\bar{\mathbf{s}})) \tag{A.1}$$

Here, the Lagrangian function is equal to the objective function for zero residuals, i.e., $\mathbf{r}(\bar{\mathbf{s}}, \mathbf{v}(\bar{\mathbf{s}})) = \mathbf{A}\mathbf{v} - \mathbf{h}$. The derivative of the Lagrangian with respect to the vector of level set variables $\bar{\mathbf{s}}$ is written following the chain rule

$$\begin{aligned}\frac{\mathrm{d}\mathcal{L}}{\mathrm{d}\bar{\mathbf{s}}} &= \frac{\partial \mathcal{C}}{\partial \bar{\mathbf{s}}} + \frac{\partial \mathcal{C}}{\partial \mathbf{v}}\frac{\partial \mathbf{v}}{\partial \bar{\mathbf{s}}} + \boldsymbol{\lambda}^T \left(\frac{\partial \mathbf{r}}{\partial \bar{\mathbf{s}}} + \frac{\partial \mathbf{r}}{\partial \mathbf{v}}\frac{\partial \mathbf{v}}{\partial \bar{\mathbf{s}}}\right) \\ &= \frac{\partial \mathcal{C}}{\partial \bar{\mathbf{s}}} + \boldsymbol{\lambda}^T \frac{\partial \mathbf{r}}{\partial \bar{\mathbf{s}}} + \underbrace{\left(\frac{\partial \mathcal{C}}{\partial \mathbf{v}} + \boldsymbol{\lambda}^T \frac{\partial \mathbf{r}}{\partial \mathbf{v}}\right)}\frac{\partial \mathbf{v}}{\partial \bar{\mathbf{s}}}\end{aligned} \tag{A.2}$$

In order to avoid the costly calculation of the derivatives of the state, the Lagrange multiplier can be chosen such that the underlined term vanishes. Thus the adjoint equation is written as:

$$\mathbf{A}^T \boldsymbol{\lambda} = -\left(\frac{\partial \mathcal{C}}{\partial \mathbf{v}}\right)^T \tag{A.3}$$

For complex state variables the source term of the adjoint equation is calculated as the following [6]:

$$\frac{\partial \mathcal{C}}{\partial \mathbf{v}} = \frac{\partial \mathcal{C}}{\partial \mathbf{v}_r} - \mathrm{i}\frac{\partial \mathcal{C}}{\partial \mathbf{v}_i} \tag{A.4}$$

Where the real and the imaginary parts of a complex number are denoted by subscripts r and i, respectively. After calculating the Lagrange variables that satisfy the adjoint equation, the gradient is evaluated as:

$$\frac{\mathrm{d}\mathcal{C}}{\mathrm{d}\bar{\mathbf{s}}} = \frac{\partial \mathcal{C}}{\partial \bar{\mathbf{s}}} + \Re\left(\boldsymbol{\lambda}^T \frac{\partial \mathbf{A}}{\partial \bar{\mathbf{s}}}\mathbf{u} - \frac{\partial \mathbf{h}}{\partial \bar{\mathbf{s}}}\right) \tag{A.5}$$

In the level set based cut element framework, the design evolves from the zero contour of the level set field. This implies that, the sensitivity information is only available from the cut elements and variation of design variables elsewhere do not effect the state variables. Consequently, the above sensitivity equation (Eq. A.5) is only evaluated at the elements that are marked as cut. The parametrization thus results in very localized sensitivities. This is the main reason behind the usage of filtering techniques on design variables which essentially increases the zone of influence of the design sensitivities. We compute the partial derivatives of the system matrix with respect to the level sets $\frac{\partial \mathbf{A}}{\partial \bar{\mathbf{s}}}$ using a simple central difference scheme. These are computed on element level by by perturbing nodal level set values with $|\bar{s}_i|/10^5$ and integrating the local matrices with the modified cut configuration. If the source $\mathbf{h}$ is also design dependent, the same finite difference procedure is applied to calculate $\frac{\partial \mathbf{h}}{\partial \bar{\mathbf{s}}}$. Analytical formulas for the sensitivities can be derived, see e.g. Bernland et.al.[28], however, following the conclusions of Sharma et.al.[61] we choose the semi-discrete approach as this is computationally more efficient and because it does not introduce any noteworthy error.

To obtain the gradient with respect to the mathematical design variables $\mathbf{s}$ the following chain rule is applied.

$$\frac{\mathrm{d}\mathcal{C}}{\mathrm{d}\mathbf{s}} = \frac{\mathrm{d}\mathcal{C}}{\mathrm{d}\bar{\mathbf{s}}}\frac{\partial \bar{\mathbf{s}}}{\partial \bar{\mathbf{s}}_\mathbf{c}}\frac{\partial \bar{\mathbf{s}}_\mathbf{c}}{\partial \tilde{\mathbf{s}}_\mathbf{c}}\frac{\partial \tilde{\mathbf{s}}_\mathbf{c}}{\partial \tilde{\mathbf{s}}}\frac{\partial \tilde{\mathbf{s}}}{\partial \mathbf{s}} \tag{A.6}$$

The chain rule is obtained by calculating the partial derivatives of the operations which link the level set to the mathematical design variables (described in section 2.2) and applying them in reverse order. All partial derivatives of the operations in the above chain rule to calculate the needed gradient are derived analytically.

The operators $\mathbf{A}_e$ and $\mathbf{A}_n$ are defined to linearly interpolate from element centers to nodes and from nodes to element centers, respectively. These operations are utilized as:

$$\mathbf{A}_e \bar{\mathbf{s}}_\mathbf{c} = \bar{\mathbf{s}}, \qquad \mathbf{A}_n \tilde{\mathbf{s}} = \tilde{\mathbf{s}}_\mathbf{c} \tag{A.7}$$

and the partial derivatives are written for completeness

$$\frac{\partial \bar{\mathbf{s}}}{\partial \bar{\mathbf{s}}_\mathbf{c}} = \mathbf{A}_e, \qquad \frac{\partial \tilde{\mathbf{s}}_\mathbf{c}}{\partial \tilde{\mathbf{s}}} = \mathbf{A}_n \tag{A.8}$$

The term $\frac{\partial \tilde{\mathbf{s}}}{\partial \mathbf{s}}$ in Eq. A.6 is the partial derivative of the linear mapping operation ($\tilde{s}_i = (h_e s_i) - 0.5 h_e$) of changing the bounds on the design variables and it is realized as a diagonal matrix $\mathbf{A}_m$ with constant entries of h_e.

The pde filter equation introduced in Eq. 2 in discrete form is written as:

$$\mathbf{D}\bar{\mathbf{s}}_\mathbf{c} = \mathbf{T}\tilde{\mathbf{s}}_\mathbf{c} \tag{A.9}$$

The system matrix $\mathbf{D}$ is a symmetric matrix from the finite volume discretization of the filter equation and $\mathbf{T}$ is a diagonal matrix which holds element volumes. The partial derivative $\frac{\partial \bar{\mathbf{s}}_{\mathbf{c}}}{\partial \tilde{\mathbf{s}}_{\mathbf{c}}}$ can then be written as:

$$\frac{\partial \bar{\mathbf{s}}_{\mathbf{c}}}{\partial \tilde{\mathbf{s}}_{\mathbf{c}}} = \mathbf{D}^{-1}\mathbf{T} \tag{A.10}$$

Here, rather than forming the inverse of the matrix $\mathbf{D}$, the following system of equations are solved

$$\mathbf{D}\ \mathbf{a} = \mathbf{A}_e^T \frac{\mathrm{d}\mathcal{C}}{\mathrm{d}\bar{\mathbf{s}}} \tag{A.11}$$

After calculating the variables $\mathbf{a}$ that satisfy the above equation, the gradient with respect to the mathematical design variables is calculated as:

$$\frac{\mathrm{d}\mathcal{C}}{\mathrm{d}\mathbf{s}} = \mathbf{A}_m \left[\mathbf{A}_n^T \left(\mathbf{T}\ \mathbf{a}\right)\right] \tag{A.12}$$

REFERENCES

[1] M. P. Bendsøe, N. Kikuchi, Generating optimal topologies in structural design using a homogenization method, Computer Methods in Applied Mechanics and Engineering 71 (2) (1988) 197–224. doi:10.1016/0045-7825(88)90086-2.
URL http://linkinghub.elsevier.com/retrieve/pii/0045782588900862

[2] M. P. Bendsøe, Optimal shape design as a material distribution problem, Structural optimization 1 (4) (1989) 193–202. doi:10.1007/BF01650949.
URL https://doi.org/10.1007/BF01650949

[3] N. Aage, E. Andreassen, B. S. Lazarov, O. Sigmund, Giga-voxel computational morphogenesis for structural design, Nature 550 (7674) (2017) 84–86. doi:10.1038/nature23911.

[4] C. B. Dilgen, S. B. Dilgen, D. R. Fuhrman, O. Sigmund, B. S. Lazarov, Topology optimization of turbulent flows, Computer Methods in Applied Mechanics and Engineering 331 (2018) 363 – 393. doi:https://doi.org/10.1016/j.cma.2017.11.029.
URL http://www.sciencedirect.com/science/article/pii/S0045782517307478

[5] E. A. Kontoleontos, E. M. Papoutsis-Kiachagias, A. S. Zymaris, D. I. Papadimitriou, K. C. Giannakoglou, Adjoint-based constrained topology optimization for viscous flows, including heat transfer, Engineering Optimization 45 (8) (2013) 941–961. arXiv:https://doi.org/10.1080/0305215X.2012.717074, doi:10.1080/0305215X.2012.717074.
URL https://doi.org/10.1080/0305215X.2012.717074

[6] M. B. Dühring, J. S. Jensen, O. Sigmund, Acoustic design by topology optimization, Journal of Sound and Vibration 317 (3-5) (2008) 557–575. doi:10.1016/j.jsv.2008.03.042.

[7] E. Wadbro, M. Berggren, Topology optimization of an acoustic horn, Computer Methods in Applied Mechanics and Engineering 196 (1-3) (2006) 420–436. doi:10.1016/j.cma.2006.05.005.

[8] O. Sigmund, P. M. Clausen, Topology optimization using a mixed formulation: An alternative way to solve pressure load problems, Computer Methods in Applied Mechanics and Engineering 196 (13-16) (2007) 1874–1889. doi:10.1016/j.cma.2006.09.021.

[9] B. Bourdin, Filters in topology optimization, International Journal for Numerical Methods in Engineering 50 (9) (2001) 2143–2158. doi:10.1002/nme.116.

[10] T. E. Bruns, D. A. Tortorelli, Topology optimization of non-linear elastic structures and compliant mechanisms, Computer Methods in Applied Mechanics and Engineering 190 (26-27) (2001) 3443–3459. doi:10.1016/S0045-7825(00)00278-4.

[11] J. K. Guest, J. H. Prévost, T. Belytschko, Achieving minimum length scale in topology optimization using nodal design variables and projection functions, International Journal for Numerical Methods in Engineering 61 (2) (2004) 238–254. doi:10.1002/nme.1064.

[12] F. Wang, B. S. Lazarov, O. Sigmund, On projection methods, convergence and robust formulations in topology optimization, Structural and Multidisciplinary Optimization 43 (6) (2011) 767–784. doi:10.1007/s00158-010-0602-y.

[13] C. B. Dilgen, S. B. Dilgen, N. Aage, J. S. Jensen, Topology optimization of acoustic mechanical interaction problems: a comparative review, Structural and Multidisciplinary Optimization 60 (2) (2019) 779–801. doi:10.1007/s00158-019-02236-4.
URL https://doi.org/10.1007/s00158-019-02236-4

[14] S. Osher, J. Sethian, Fronts propagsting with curvature-dependent speed - algorithms based on hamilton-jacobi formulations, Journal of Computational Physics 79 (1) (1988) 12–49. doi:10.1016/0021-9991(88)90002-2.

[15] J. A. Sethian, A. Wiegmann, Structural boundary design via level set and immersed interface methods, Journal of Computational Physics 163 (2) (2000) 489–528. doi:10.1006/jcph.2000.6581.

[16] H. Isakari, K. Kuriyama, S. Harada, T. Yamada, T. Takahashi, T. Matsumoto, A topology optimisation for three-dimensional acoustics with the level set method and the fast multipole boundary element method, Mechanical Engineering Journal 1 (4) (2014) CM0039–CM0039. doi:10.1299/mej.2014cm0039.

[17] Y. Noguchi, T. Yamamoto, T. Yamada, K. Izui, S. Nishiwaki, A level set-based topology optimization method for simultaneous design of elastic structure and coupled acoustic cavity using a two-phase material model, Journal of Sound and Vibration 404 (2017) 15–30. doi:10.1016/j.jsv.2017.05.040.

[18] G. Allaire, F. Jouve, A. M. Toader, Structural optimization using sensitivity analysis and a level-set method, Journal of Computational Physics 194 (1) (2004) 363–393. doi:10.1016/j.jcp.2003.09.032.

[19] S. Wang, M. Y. Wang, Radial basis functions and level set method for structural topology optimization, International Journal for Numerical Methods in Engineering 65 (12) (2006) 2060–2090. doi:10.1002/nme.1536.

[20] G. Allaire, C. Dapogny, P. Frey, Shape optimization with a level set based mesh evolution method, Computer Methods in Applied Mechanics and Engineering 282 (2014) 22–53. doi:10.1016/j.cma.2014.08.028.

[21] L. Shu, M. Yu Wang, Z. Ma, Level set based topology optimization of vibrating structures for coupled acoustic-structural dynamics, Computers and Structures 132 (2014) 34–42. doi:10.1016/j.compstruc.2013.10.019.

[22] H. Isakari, T. Kondo, T. Takahashi, T. Matsumoto, A level-set-based topology optimisation for acoustic–elastic coupled problems with a fast bem–fem solver, Computer Methods in Applied Mechanics and Engineering 315 (2017) 501 – 521. doi:https://doi.org/10.1016/j.cma.2016.11.006. URL http://www.sciencedirect.com/science/article/pii/S0045782516305187

[23] J. Desai, A. Faure, G. Michailidis, G. Parry, R. Estevez, Topology optimization in acoustics and elasto-acoustics via a level-set method, Journal of Sound and Vibration 420 (2018) 73–103. doi:10.1016/j.jsv.2018.01.032.

[24] A. Hansbo, P. Hansbo, A finite element method for the simulation of strong and weak discontinuities in solid mechanics, Computer Methods in Applied Mechanics and Engineering 193 (33-35) (2004) 3523–3540. doi:10.1016/j.cma.2003.12.041.

[25] E. Burman, S. Claus, P. Hansbo, M. G. Larson, A. Massing, Cutfem: Discretizing geometry and partial differential equations, International Journal for Numerical Methods in Engineering 104 (7) (2015) 472–501. doi:10.1002/nme.4823.

[26] T. P. Fries, T. Belytschko, The extended/generalized finite element method: An overview of the method and its applications, International Journal for Numerical Methods in Engineering 84 (3) (2010) 253–304. doi:10.1002/nme.2904.

[27] E. Burman, D. Elfverson, P. Hansbo, M. G. Larson, K. Larsson, Shape optimization using the cut finite element method, Computer Methods in Applied Mechanics and Engineering 328 (2018) 242–261. doi:10.1016/j.cma.2017.09.005.

[28] A. Bernland, E. Wadbro, M. Berggren, Acoustic shape optimization using cut finite elements, International Journal for Numerical Methods in Engineering 113 (3) (2018) 432–449. doi:10.1002/nme.5621.

[29] M. J. De Ruiter, F. Van Keulen, Topology optimization using a topology description function, Structural and Multidisciplinary Optimization 26 (6) (2004) 406–416. doi:10.1007/s00158-003-0375-7.

[30] S. Kreissl, K. Maute, Levelset based fluid topology optimization using the extended finite element method, Structural and Multidisciplinary Optimization 46 (3) (2012) 311–326. doi:10.1007/s00158-012-0782-8.

[31] C. H. Villanueva, K. Maute, Density and level set-xfem schemes for topology optimization of 3-d structures, Computational Mechanics 54 (1) (2014) 133–150. doi:10.1007/s00466-014-1027-z.

[32] P. Liu, Y. Luo, Z. Kang, Multi-material topology optimization considering interface behavior via XFEM and level set method, Comput. Methods Appl. Mech. Eng. 308 (2016) 113–133. doi:10.1016/j.cma.2016.05.016. URL http://dx.doi.org/10.1016/j.cma.2016.05.016https://linkinghub.elsevier.com/retrieve/pii/S0045782516303802

[33] P. Coffin, K. Maute, A level-set method for steady-state and transient natural convection problems, Structural and Multidisciplinary Optimization 53 (5) (2016) 1047–1067. doi:10.1007/s00158-015-1377-y.

[34] C. H. Villanueva, K. Maute, Cutfem topology optimization of 3d laminar incompressible flow problems, Computer Methods in Applied Mechanics and Engineering 320 (2017) 444–473. doi:10.1016/j.cma.2017.03.007.

[35] A. A. Novotny, J. Sokołowski, Topological Derivatives in Shape Optimization, Springer-Verlag Berlin Heidelberg, 2013.

[36] H. Lian, A. N. Christiansen, D. A. Tortorelli, O. Sigmund, N. Aage, Combined shape and topology optimization for minimization of maximal von mises stress, Structural and Multidisciplinary Optimization 55 (5) (2017) 1541–1557. doi:10.1007/s00158-017-1656-x.

[37] X. Zhang, Z. Kang, Topology optimization of damping layers for minimizing sound radiation of shell structures, J. Sound Vib. 332 (10) (2013) 2500–2519. doi:10.1016/j.jsv.2012.12.022. URL http://www.sciencedirect.com/science/article/pii/S0022460X12009893

[38] C. Daux, N. Moës, J. Dolbow, N. Sukumar, T. Belytschko, Arbitrary branched and intersecting cracks with the extended finite element method, International Journal for Numerical Methods in Engineering 48 (12) (2000) 1741–1760. doi:10.1002/1097-0207(20000830)48:12<1741::AID-NME956>3.0.CO;2-L.

[39] A. Düster, J. Parvizian, Z. Yang, E. Rank, The finite cell method for three-dimensional problems of solid mechanics, Computer Methods in Applied Mechanics and Engineering 197 (45-48) (2008) 3768–3782. doi:10.1016/j.cma.2008.02.036.

[40] C. S. Andreasen, M. O. Elingaard, N. Aage, Level set topology and shape optimization by density methods using cut elements with length scale control, Structural and Multidisciplinary Optimization 62 (2) (2020) 685–707. doi:10.1007/s00158-020-02527-1.

[41] C. B. Dilgen, N. Aage, Generalized shape optimization of transient vibroacoustic problems using cut elements, International Journal for Numerical Methods in Engineering.

[42] P. Coffin, K. Maute, Level set topology optimization of cooling and heating devices using a simplified convection model, Struct. Multidiscip. Optim. 53 (5) (2016) 985–1003. doi:10.1007/s00158-015-1343-8. URL http://link.springer.com/10.1007/s00158-015-1343-8

[43] B. S. Lazarov, O. Sigmund, Filters in topology optimization based on helmholtz-type differential equations, International Journal for Numerical Methods in Engineering 86 (6) (2011) 765–781. doi:10.1002/nme.3072.

[44] D. Makhija, K. Maute, Numerical instabilities in level set topology optimization with the extended finite element method, Structural and Multidisciplinary Optimization 49 (2) (2014) 185–197. doi:10.1007/s00158-013-0982-x.

[45] G. Pingen, M. Waidmann, A. Evgrafov, K. Maute, A parametric level-set approach for topology optimization of flow domains, Structural and Multidisciplinary Optimization 41 (1) (2010) 117–131. doi:10.1007/s00158-009-0405-1.

[46] S. Balay, W. D. Gropp, L. C. McInnes, B. F. Smith, Efficient management of parallelism in object oriented numerical software libraries, in: E. Arge, A. M. Bruaset, H. P. Langtangen (Eds.), Modern Software Tools in Scientific Computing, Birkhäuser Press, 1997, pp. 163–202.

[47] S. Balay, S. Abhyankar, M. F. Adams, J. Brown,

P. Brune, K. Buschelman, L. Dalcin, A. Dener, V. Eijkhout, W. D. Gropp, D. Kaushik, M. G. Knepley, D. A. May, L. C. McInnes, R. T. Mills, T. Munson, K. Rupp, P. Sanan, B. F. Smith, S. Zampini, H. Zhang, H. Zhang, PETSc users manual, Tech. Rep. ANL-95/11 - Revision 3.10, Argonne National Laboratory (2018).
URL http://www.mcs.anl.gov/petsc

[48] S. Balay, S. Abhyankar, M. F. Adams, J. Brown, P. Brune, K. Buschelman, L. Dalcin, A. Dener, V. Eijkhout, W. D. Gropp, D. Kaushik, M. G. Knepley, D. A. May, L. C. McInnes, R. T. Mills, T. Munson, K. Rupp, P. Sanan, B. F. Smith, S. Zampini, H. Zhang, H. Zhang, PETSc Web page, http://www.mcs.anl.gov/petsc (2018).
URL http://www.mcs.anl.gov/petsc

[49] P. R. Amestoy, I. S. Duff, J. Koster, J.-Y. L'Excellent, A fully asynchronous multifrontal solver using distributed dynamic scheduling, SIAM Journal on Matrix Analysis and Applications 23 (1) (2001) 15–41.

[50] P. R. Amestoy, A. Guermouche, J.-Y. L'Excellent, S. Pralet, Hybrid scheduling for the parallel solution of linear systems, Parallel Computing 32 (2) (2006) 136–156.

[51] W. E. Lorensen, H. E. Cline, Marching cubes: a high resolution 3d surface construction algorithm, Computer Graphics (acm) 21 (4) (1987) 163–169. doi:10.1145/37402.37422.

[52] E. Burman, Ghost penalty, Comptes Rendus Math. 348 (21-22) (2010) 1217–1220. doi:10.1016/j.crma.2010.10.006.
URL http://dx.doi.org/10.1016/j.crma.2010.10.006https://linkinghub.elsevier.com/retrieve/pii/S1631073X10002827

[53] www.comsol.com, COMSOL Multiphysics Reference Manual, version 5.5 (2020).

[54] K. Svanberg, The method of moving asymptotes—a new method for structural optimization, International Journal for Numerical Methods in Engineering 24 (2) (1987) 359–373. doi:10.1002/nme.1620240207.

[55] N. Aage, B. S. Lazarov, Parallel framework for topology optimization using the method of moving asymptotes, Structural and Multidisciplinary Optimization 47 (4) (2013) 493–505. doi:10.1007/s00158-012-0869-2.

[56] N. Aage, E. Andreassen, B. S. Lazarov, Topology optimization using petsc: An easy-to-use, fully parallel, open source topology optimization framework, Structural and Multidisciplinary Optimization 51 (3) (2015) 565–572. doi:10.1007/s00158-014-1157-0.

[57] G. H. Yoon, J. S. Jensen, O. Sigmund, Topology optimization of acoustic-structure interaction problems using a mixed finite element formulation, International Journal for Numerical Methods in Engineering 70 (9) (2007) 1049–1075. doi:10.1002/nme.1900.

[58] Q. Li, W. Chen, S. Liu, L. Tong, Structural topology optimization considering connectivity constraint, Struct. Multidiscip. Optim. 54 (4) (2016) 971–984. doi:10.1007/s00158-016-1459-5.
URL http://link.springer.com/10.1007/s00158-016-1459-5

[59] M. Bendsøe, N. Olhoff, J. Taylor, A variational formulation for multicriteria structural optimization, Journal of Structural Mechanics 11 (4) (1983) 523–544. doi:10.1080/03601218308907456.

[60] F. Jacobsen, P. M. Juhl, Fundamentals of General Linear Acoustics, John Wiley & Sons Ltd, 2013.

[61] A. Sharma, H. Villanueva, K. Maute, On shape sensitivities with heaviside-enriched XFEM, Struct. Multidiscip. Optim. 55 (2) (2017) 385–408. doi:10.1007/s00158-016-1640-x.
URL http://link.springer.com/10.1007/s00158-016-1640-x